UNIVERSITY OF COPENHAGEN
Faculty of Science

Master's Thesis

Nanoskiving InAs Nanowires for Quantum Devices

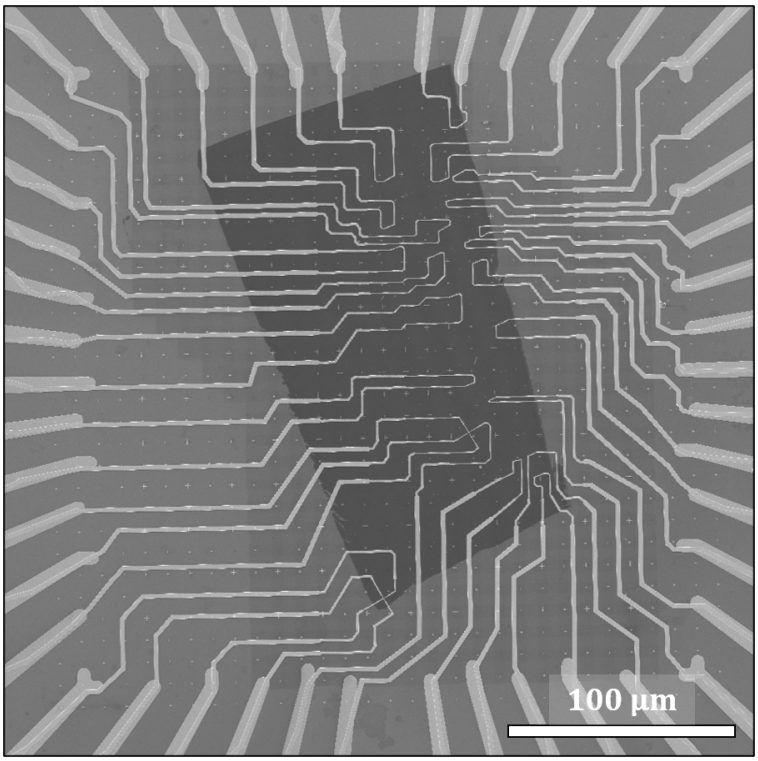

Author:
Daniel Sandager Dragheim Kjær

Supervisors:
Jesper Nygård
Joachim Sestoft
Thomas Kanne Nordqvist

Center for Quantum Devices
Niels Bohr Institute

05-09-2022

Abstract

III-V nanowires such as InAs, exhibit great carrier mobility, which makes it a suitable material for transistors. InAs also shows low contact resistance and sufficient interfacial quality for high-k dielectrics, making it of great interest for reasearch. In this thesis, the nanoskiving technique has been used to explore a relatively new platform for quantum electronics. Initial device fabrications indicated to some extend the applicability of this technique, however due to the nanowires' requirement to be embedded in an epoxy polymer, the epoxy proved difficult to handle. Indications of residual epoxy on top of the nanoskived samples appeared to be detrimental for device fabrication, which resulted in several tests of the epoxy performed by plasma ashing, and heating in order to investigate the extend of issues that the epoxy brings. Ultimately, it appeared that contamination of the epoxy was the reason for difficulties during the device fabrication, however this still remains to be seen.

Acknowledgements

I should acknowledge the following: Jesper Nygård, Joachim Sestoft, Thomas Kanne, Kasper G. R., Oscar Perstølen, Rasmus Schlosser, Daniel Ross, Mikelis Marnauza.... others????? - Joachim igen, fordi han er nice.

Karolis, Martin?

I would like to thank Jesper Nyård for this educational and highly fascinating opportunity to work in an environment with dedicated and talented people. A huge thank you to the Thomas Kanne, Joachim Sestoft and Rasmus D. Schlosser for providing great assistance and guidance when needed, as well as a good laugh every now and then. I thank Kasper Grove-Rasmussen for providing with help when needed, especially when working at the Heliox. Oscar Perstølen requires a special thank you for his for being a good student to consult. To Daniel Ross I'm thanking him for being a great study buddy throughout of the years prior to this project, but also for making me the best Daniel around at the office during the project. Mikelis Marnauza is not to be forgotten, as he taught spent the time way back to teach me the way of the microtome. To Karolis Parfeniukas and Martin Bjergfelt, great company, and great guys.

A general appreciation of everyone at QDev for their friendly and helpful attitudes. Also, the coffee machines in the lounges, I thank you for your services.

Paldies jums visiem!

Contents

1 Introduction

Semiconductor nanostructures have attracted plenty of attention due to their unique physical properties towards technological applications, and in particular III-V nanowires because they exhibit intrinsic high carrier mobilities[8], gateability[47], as well as high surface-to-volume ratios, which makes them attractive for high performance sensers. Especially, InAs attracts attention due to its direct band gap and high electron mobility making it a promising candidate for nanowire-based transistors, and photovoltaics.[58]

The strive for development of nanowires to be incorporated into large scale devices requires, control of shape, sizes, and control of position of devices in form of arrays. In addition a reproducible and reliable method of method is required providing viable alternatives in terms of cost.[3] Hence, the nanoskiving approach with the ability to cut several lamellae containing a structured and flexible array of nanocrystals for devices purposes can potentially provide an alternative route for scalability.

Several uses of the microtome for nanowire characterization has been done[12, 56], however despite in ref [41], the use of nanoskiving towards quantum electronics is still unexplored.

2 Electron transport phenomena

The two main electron transport phenomena observed in this work are that of a quantum dot, and Fabry-Pérot interferrometer.

2.1 Quantum dot

A quantum dot is a small confined region in space, which is able to contain a finite number of electrons. For a structure to exhibit this property some conditions are required. The quantization of electrons on the quantum dot requires sufficiently large tunneling barrier, which is to say that the system needs to be weakly coupled to its surroundings, e.g. leads.

This translates into the energy required to charge the dot by one electron needs to be much larger than the energy uncertainty. As a consequence, by means of heisenberg's uncertainty principle, the tunneling resistance must be

$$R_t >> \frac{h}{e^2} \tag{1}$$

Hence, this implies that the system has to be deep in the tunneling regime.there is a charging (or discharging) time for an electron, meaning the electron has a lifetime. In other words, low uncertainty of where the electron is.

A second important criteria is that the charging energy must be much larger than the thermal energy

$$E_C = \frac{e^2}{C} >> k_B T \tag{2}$$

This condition can be fulfilled by having a small dot, as the self-capacitance of an object is directly proportional to its size. If the temperature is small compared to the single-particle level spacing then quantized energy levels can contribute to the conductance.

However, such systems in general require the dimension of the system to be small enough for the confinement energy to dominate.

Due to the dot being capacitively coupled to its surroundings a plunger gate can continuously change the electrostatic potential in contrast to the discontinuous charging energy an electron provides by means of tunneling on or off the dot. A qualitative description of a quantum dot is depticted in **Fig. 1**. In a small bias window, which depend on the differences of the source and drain chemical potentials, electron tunneling is on resonance when an energy level is within the bias window **(a)**. By electrostatically gating the energy levels can be shifted in energy. A positive voltage will pull the chemical potential down. When there is no energy level within the bias window, we talk about Coulomb blockade, and the tunneling is suppressed **(b)**. Further electrostatic gating will eventually result in an energy level yet again entering the bias window **(c)**.

This qualitative description forms the basis for the Coulomb blockade phenomenon. Furthermore, by increasing the bias window in the coulomb region, the bias voltage at which current starts flowing again is the energy between the individual levels, called the addition energy (i.e. the energy required to add/remove an electron to/from the dot) and is a combination of $E_{add} = e^2/C + \Delta E$ the charging energy and the confinement energy that is the level spacing ΔE. Since the gate voltage changes the electrostatic energy on the dot, also this quantity can change the occupation of the dot by

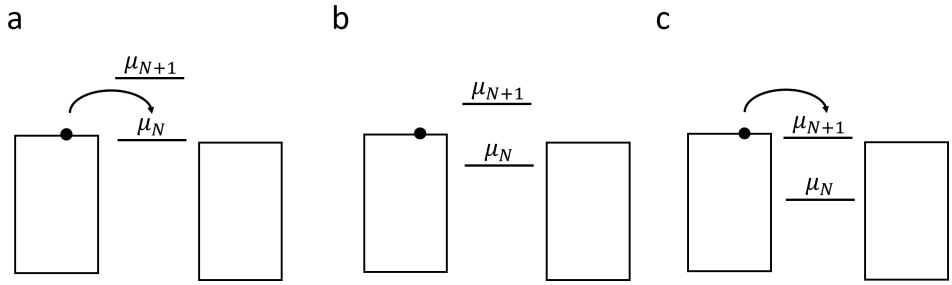

Fig. 1: Qualitative depiction of a quantum dot.The quantized energy levels on the quantum dot can by means of electrostatic gating be modulated. In (a) the energy level is within the bias window, which result in single electron tunneling from the the lead to the dot. In (b) the energy level μ_N is occupied, and tunneling is suppressed. In (c) further positive gating result will eventually pull the energy level of μ_{N+1} into the bias window where tunneling once again is possible

$$\Delta V_g = \frac{C}{eC_g} \cdot (\Delta E + e^2/C) \tag{3}$$

where C/C_g is the conversion factor, C is the total capacitance of the system, C_g is the gate capacitance, and inside of the parenthesis is the addition energy.

Hence, varying both the bias voltage and the gate voltage, is able to form bias-spectroscopy plots of Coulomb diamonds.

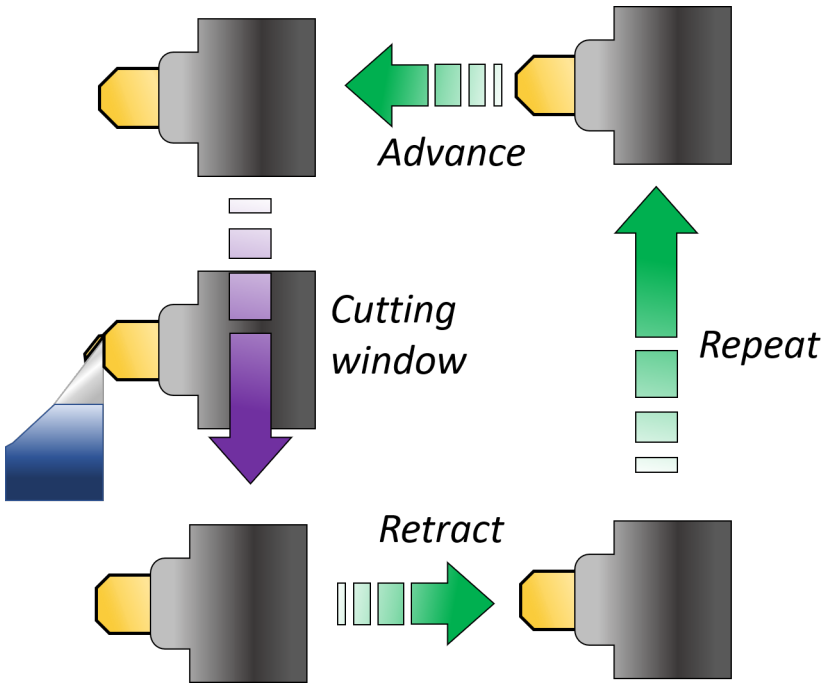

Fig. 2: Cyclic motion. The schematic depicts the repeating cycle of the sample holder motion. In ints initial position it advances towards the knife, and then moves downards. Within the set cutting window (purple arrow), the speed of the motion declines to the one that is desired. If the sample is close enough to the diamond knife, the knife will cut a section off it producing a lamella. Afterwards the sample retracts, and starts the process all over.

3 Microtomy

The Leica Ultracut UCT Microtome is an instrument routinely used to prepare biological samples for electron microscopy investigation. It requires embedding of the sample in an epoxy resin to-be hardened, followed by sectioning with a diamond knife. The power of the Microtome is to prepare extremely thin sections, or lamellae, in the nanometer range of 10 nm to 200 nm with a highly precise increment movement of the attached knife.

3.1 Tool setup

The instrument consists of three major components: One, is the knife stage which is a static stage once the automated process of sectioning is going, the other is the sample holder, which moves in a cyclic motion going up and down while also moving horizontally in the direction of the knife. The third is the stereoscope which is angled with respect to the built-in light source such that the observed color of the sectioned lamella represents a certain thickness.

3.2 Microtome working principle

The basic working principle of the microtome is illustrated in **Fig. 2**. The illustration is simplified as there is no water depicted in the knife boat, and since the actual motion of the sample holder is elliptical, and does not move in straight lines. Nevertheless, the sample is loaded in the sample holder, which moves in a repeated cycle of advancement towards the diamond knife, followed by a downwards motion moving past the knife. If the sample is sufficiently close, then a section will be cut from the sample, which will then float on the water. The sample holder then retracts away from the knife. The movement is then repeated.

The cutting window is manually set on the microtome console. It is in this window, where one expects the knife to cut through the sample with a regulated speed also set on the console. After a lamella has been cut the interference of the light source with the lamella and water result in a certain color which can be translated into an approximate thickness. A golden color is typically an indication of a lamella thickness of 100 nm.

3.3 Alignment Procedure

The alignment procedure requires as clean and reflective surface on the sample block face, since the reflection of the diamond knife edge is used for alignment. As depicted in **Fig. 3**, two types of alignments are required to adjust. There is a horizontal alignment, which reqmuires the knife edge to be parallel to the block face surface. In order to do so, one needs to align the knife edge reflection such that it is parallel to the actual knife.

The second type of alignment is a vertical one. Here the sample is aligned with respect to the knife, and is done by rotating the sample as illustrated by the arrows, on the right-hand side of the figure. The *side views* illustrates this point. The front *front views* corresponds to the shown side views. The vertical alignment also requires attention to the reflection, where one needs to look out for whether the dark area stays in size across the block face, or whether it appears to be "growing". If growing one needs to accommodate that by adjusting the sample in the opposite direction of the dark area growth.

4 Preparing nanowires for nanocrystal devices

The process of manufacturing cross-sections (CSs) of nanowires (NWs) for quantum devices consists of several steps even before traditional fabrication processing can occur. The NWs has to be prepared, which requires manual cleaving of the growth substrate *(1)* in order to fit the samples into the silicone mold used for embedding *(2)* of the NWs in an epoxy resin, which subsequently has to be baked *(3)* for hardening of the resin matrix.

At this point the sample is ready for microtomy. Here, the sample needs further manipulation, which consists of *(4)* removal of the growth substrate in order to get access to the embedded NWs, followed by *(5)* the actual cutting process of the them.

The sample can then be *(6)* transferred to various kinds of substrates, such as the device substrate. At this point, the sample has been fully prepared and all that is left, is to fabricate the devices *(7)*.

In this chapter a detailed description of the entire processing and manipulation of NWs into cross-sectioned NWs is accounted for, starting with the very first step: Nanowire preparation.

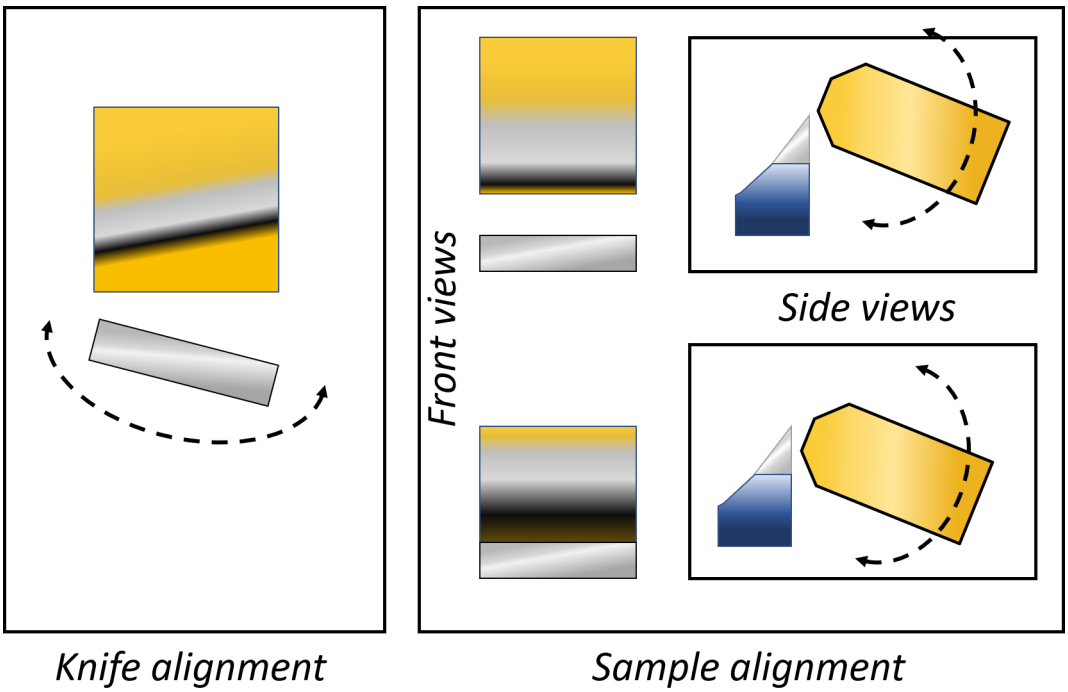

Fig. 3: Sample alignment. One distinguishes two different alignments. The first one is depicted on the left-hand side. Here the knife is rotated horizontally, and the resulted reflection of the knife edge (black area) is projected onto the block face of the sample accordingly. The grey color scheme on the block face is the reflection of the water in the trough. On the right-hand side, the second type of alignment is depicted. Here one adjusts the vertical alignment of the sample with respect to the knife, by means of observing the reflection on the block face. Is the sample aligned as depicted in the *side views*, then the knife edge reflection will "grow" as the sample is moved past the knife.

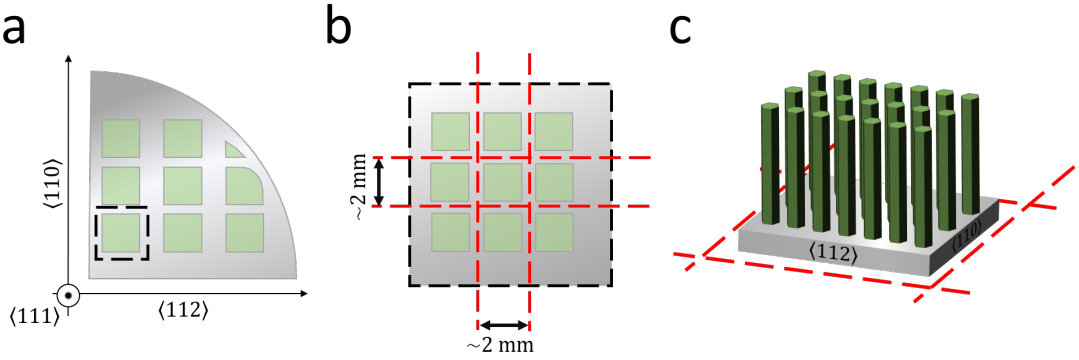

Fig. 4: Cleaving the growth substrate. In (a) an InAs ⟨111⟩B quarter-inch wafer is displayed with green squares representing several even smaller NW arrays, as indicated by the dashed, black square, which consequently is enlarged in (b). The desired target NW array is scribed, and subsequently cleaved along the wafers crystal planes, resulting in a small piece of the substrate (c) not much larger than $\sim 2 \times 2$ mm. The red dashed lines represent cleaving

4.1 Sample preparation of nanowires

The preparation of the NWs entails affixing them into a polymer matrix in order to stabilize the free-standing NWs upon cutting them into cross-sections. Hence, entire pieces of the InAs ⟨111⟩B growth substrate is cut into smaller pieces of $\sim 2 \times 2$ mm. Inside of such an area, are 25 even smaller arrays, each with an approximate size of $\sim 250 \times 250 \mu$m. Each of these 25 arrays are similar, but vary in one aspect. For the case of NWs grown in close proximity to each other, the inter-NW distances was varied in order to find optimal parameters of conjoined NWs.

As a result a manual scriber with a diamond head is used to make scribe marks along the direction of the crystallographic planes as indicated in **Fig. 4**. On a quarter-inch wafer containing various NW arrays, the target array is located **(a)** and consequent scribe marks are made as denoted by the dashed red lines in **(b)**. A single scribe line in either direction applied with the highest force is sufficient in order to easily cleave the marked arrays into pieces of proper sizes **(c)**.

The next step is to carefully embed the cleaved substrates in a polymer matrix. It is important that each component consisting of the polymer epoxy resin is weighted and proportioned properly in order to form a sufficiently strong matrix after curing. The mixture will consist of mainly low-viscosity compounds, which helps with infiltration of the embedded sample into the matrix. The epoxy consists of four different compounds: A cross-linker, flexibilizer, hardener and an accelerator. The names are close-to self-explanatory, however, a short description is rightfully in place. Each component is vital, although some more than others. The job of the cross-linker is to reduce the viscosity of the entire mixture by forming a large network between the other compounds. On its own, this compound will result in incredibly hard samples, but with a flexibilizer, which easily becomes an integral part of the network, the hardness is lowered. Although, too much of the flexibilizer and the sample will become brittle, which reduces its applicability towards microtomy. The hardener is also known as the curing agent, and is the curing catalyst, which in combination with the cross-linker forms a large network of cross-linked polymers, increasing the mechanical properties. The last compound of the mixture is the accelerator. This compound is not strictly

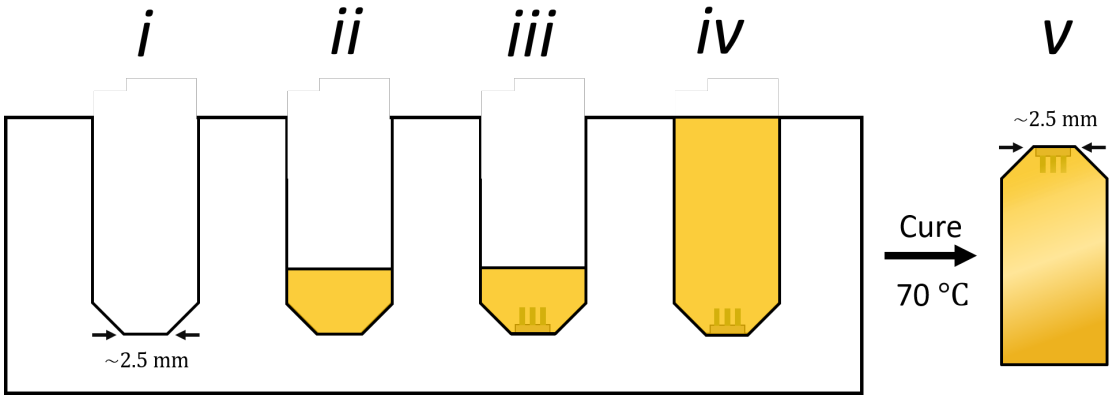

Fig. 5: Substrate embedding. A silicone mold is used as a casting to form bullet-shaped epoxy samples containing the NW substrate. Step *(i)* is an empty casting with a surface area at the bottom of roughly $\sim 2.5 \times 2.5$ mm. Step *(ii)* is creating a cushion of the epoxy resin, which allows larger control of the substrate descend *iii.* The following step is to completely fill the casting *(iv)*, followed by curing at 70°C *(v)*

necessary, but it sufficiently decreases the curing time of the sample, and in most cases limits the curing time requirement to 8 hours, or as an over-night curing[44],[14].

Having carefully prepared the epoxy mixture, swift but accurate placement of the cleaved NW substrates is of the essence due to the hardeners susceptibility towards reacting with atmospheric moisture. In **Fig. 5** the process of embedding the NWs in a silicone casting is shown. In an empty casting *(i)*, the first step is to form a cushion of the epoxy mixture in the bottom of the mold *(ii)* in order to control the descend of the substrate *(iii)*, and finally the bullet-shaped casting is filled to the top *(iv)*, after which the final step is to harden *(v)* the mixture by curing the sample at 70°C for a minimum of 8 hours as per the original recipe of A. R. Spurr in ref. [44].

However, the curing time can vary quite significantly if one is not careful in the epoxy resin mixing phase, due to improper mixture stoichiometry. Optimal curing times appeared to be in the range of 16 to 24 hours, resulting in hard bullets of epoxy.

At this point the sample is close to being properly prepared in order to start cutting the sample into thin sections, known as lamellae, containing cross-sectioned NWs in the form of nanocrystals (NC). The remaining part before the microtome set-up is put into action, is to remove the substrate, as shown with the close-ups of the bullet-like shaped epoxy samples in **Fig. 6**. As the NWs point inwards, a simple removal of the substrate will result in a clean and reflective surface ready for sectioning. Initially *(i)*, a razor blade is used to manually remove excess epoxy, which opens up for removal by gently wiggling the razor blade just below the substrate left and right all around the substrate. When sufficient material has been removed, and incisions have been made all around the substrate *(ii)*, then by gently wiggling the razor blade up and down will eventually make the growth substrate fly off with a popping sound *(iii)*. As the substrate is removed, more trimming of the sample is required in order to narrow down the surface. One needs to be aware that sufficiently large surfaces - also known as block faces - tend to result in wrinkled lamellae, or in worst case, a wet block face. If wet, then cutting the lamella is impossible as the sections will stick to the sample

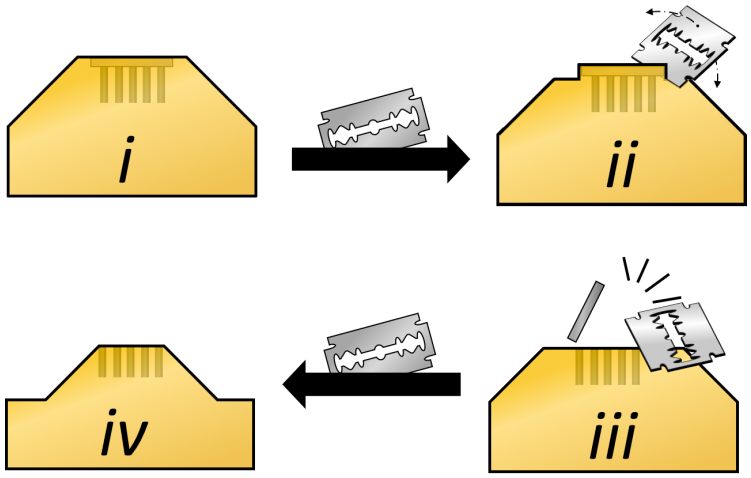

Fig. 6: Trimming and substrate removal. The cured epoxy sample containing the NW substrate requires a final manipulation before the cutting process can start. In *(i)* a close-up of the cured sample is presented. A razor blade is used to remove the epoxy surrounding the growth substrate *(ii)*, such that incisions around it can be made to easily remove the substrate *(iii)*. Further trimming all the way down to the NW array is done *iv)*

surface, and be dragged past the knife-edge. Hence decreasing the block face as much as possible will help sectioning performance. The size of a single NW array is approximate $250 \times 250 \mu$m, which usually works fine.

4.2 Transferring lamellae to substrates

The working principles of the microtome is discussed in the previous section 3, which includes movement of the sample holder-arm, and sample alignment to the knife-boat. Hence, the alignment procedure will be skipped, and this section will begin with lamellae, which are already sectioned. For examples of badly aligned samples, see the Appendix.

Upon successful sectioning of the epoxy sample, a thin lamella of ~ 100 nm floats on the water in the knife boat, as illustrated in **Fig. 7 (a)**. Here three lamellae are pictured, and numbered in order of sectioning. Transfers of three lamellae to various substrates, such as a Si substrate *(1)* for SEM or AFM purposes, or to a highly-doped Si substrate for device fabrication *(2)*, or even a transmission electron microscopy (TEM) carbon-coated copper grid *(3)*, are shown in the insets. Two essential tools are required. One is a tweezer, and the second is a stick with an eyebrow glued to it, see **Fig. 7 (b)**. The reason for the eyebrow-stick is to help guide the lamella into place, though care is needed as lamella tend to collapse around the eyebrow if sufficiently force is exerted onto the lamella.

The surface tension of the water can be of great help to correctly transfer the lamella to a substrate. By holding the substrate such that a convex meniscus is formed between the substrate and the water increases transfer control. The surface tension helps to guide the lamella by increasing

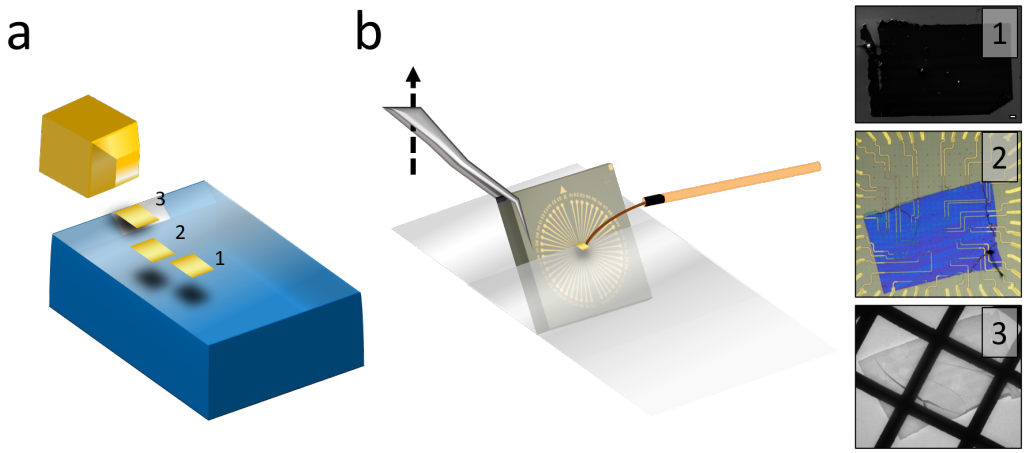

Fig. 7: Lamella transferring. Three sectioned lamellae are depicted in the trough floating on top of the water (a). To transfer a lamellae to a substrate; one hand dips the substrate into the water, whereas the second hand uses a stick with an eyebrow glued to it to guide the lamella into proper position. The collumn to the right shows the successful transfer of lamella to three different substrates. The lamella marked with "1" is transferred to a Si substrate for SEM imaging. The lamella marked with "2" is transferred to a device substrate, and the lamella marked with "3" is transferred to a transmission electron microscopy grid.

by aiding in sticking of the lamella to the surface of the substrate. Thus, simply pulling the substrate upwards in a slow and controlled manner will make it stick to the substrate minimizing the risk of lamella folding or wrinkling. The result of such lamella handling is seen in the three insets each labelled with a number corresponding to the order of sectioning.

From this point onwards, the device fabrication can beginfollows traditional processing as one would do for NWs. However, as traditional as the fabrication process is, there were issues, which to a large degree is expected to stem from the epoxy lamella itself. In the following chapters the issues and challenges of working with this kind of material will be presented, while relating its applicability towards device fabrication.

5 Issues Inhibiting Device Fabrication

In this chapter some of the unique properties of working with the NC platform will be highlighted along with the effect on device fabrication. The observations on display in this chapter serve as the groundwork for optimizing device fabrication processing, with the aim of hopefully increasing the amount of successfully functioning devices. It should be mentioned that in the following the main source of the issues most likely originates from chemical degradation likely due to contamination. This epoxy mixture serves as the base for microtomy, as discussed in the previous chapter. Due to degraded chemical properties the hardness of the cured mixture tends to be less than hoped, hence continuously altering the curing time was necessary, but in most cases was a *re*action, rather than a preventive action. It should be mentioned that off-stoichiometric mixing conditions can have the

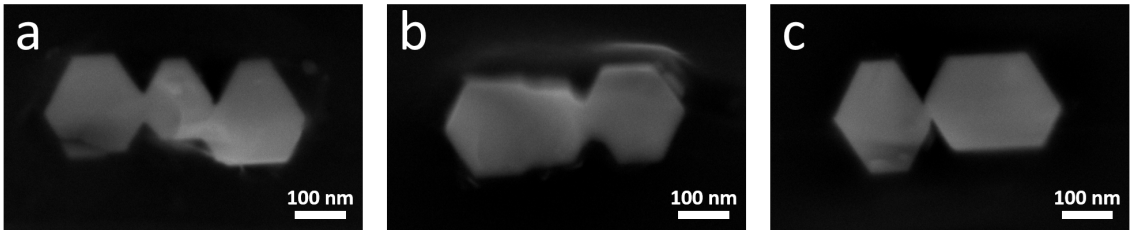

Fig. 8: Contrast indication of soft epoxy. Scanning electron microscopy micrographs of three NC structures exhibiting various extend of contrast on top and besides them. On the structure in (a) there is contrast on top of the structure. In (b) contrast is besides the structure, and in (c) no white contrast is present.

same effect. Unless the quality of the samples are way off, then microtomy can handle a degraded sample, but not necessarily so for device fabrication. This means the contamination can be hidden, and unless something out of the ordinary is observed, can remain a secret.

This chapter will begin with this out-of-the-ordinary observation, and will evolve into a deeper investigation of the challenges that degradation poses on fabrication steps.

5.1 Indication of nanocrystal epoxy coverage

Initially there were no signs of lamella issues. Previous in-house work performed by J. Sestoft *et al.*, 2022, did not report on any issues regarding fabrication of devices, and followed traditional fabrication processing, as we will discuss in the next chapter[41]. However, consistent device performance issues has haunted the work, which lead to plenty of troubleshooting. In **Fig. 8** three different NCs originating from the same lamella show varying contrast on, and around each structure. The first NC structure **(a)** exhibit cobweb-like contrast around it as well as on top of it. The second NC structure **(b)** appears to mostly have contrast around it, while the third NC structure **(c)** does not show any clear or similar signs as the other two. The contrast in the SEM is mostly due to compositional and topographical differences of the inspected surface. Since polymer compounds are considerably lower in atomic weight than InAs, then it is assumed the contrast variations, as mentioned on each of the structures, can be attributed to height variations.

In order to illuminate what is going on, Atomic Force Microscopy (AFM) is used to probe the surface topography of each of the three samples. A constant-height mode is used, which keeps the AFM-tip at a constant height away from the surface, which in turn also minimizes the risk of touching the surface with the tip. In **Fig. 9 (a,c,e)** each of the three NC structures are probed after the SEM images were taken. The insets at the top show optical images of the lamella. The topographic 3D height map of each structure, all show undefinable structures, except for the last one (**Fig. 9(e)** and **Fig. 8**(c), correspondingly).

The AFM topographical maps in **Fig. 9(b,d,f)** show the effect of plasma ashing for a combined of 4 minutes. Initial observations indicate that all of the NC structures had some residues on top of them, even for the third structure shown in **(e,f)**. This is interesting, as the SEM image (see **Fig. 8(c)**) of this particular NC structure did not show any clear indications of this. For the two other NC structures it is easier to see.

The first takeaway is that in the SEM using an acceleration voltage of 5 kV is not sufficient to

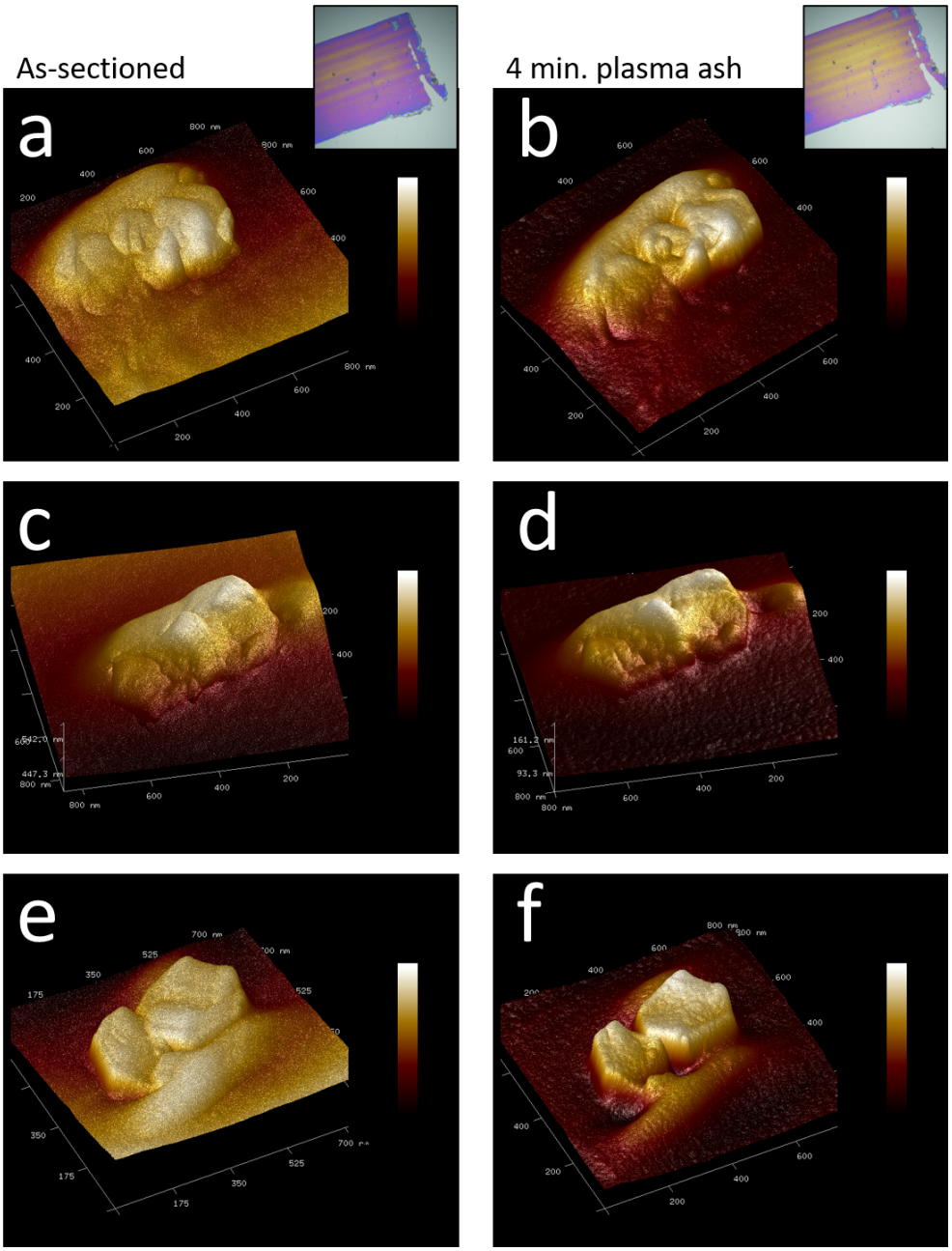

Fig. 9: Observation of residues. (a,c,e) show AFM topographic 3D representations of different NC structures as they were sectioned, although with SEM images taken before AFM probing. (b,d,f) show the same NC structures as in (a,c,e), but after 4 minutes of plasma ashing, respectively. The insets correspond to the lamella before and after ashing, respectively.

properly visualize whether there is any residuals on that might block the electrode contact. or if it is expected to be a problem as devices are fabricated. A second point is that the compositional contrast of InAs dominates over topographic contrast in the SEM. Additionaly, it is clear from the AFM topographical maps that during the sectioning process, the knife aligning was slightly off resulting in cross-sectioned NWs with uneven surfaces.

Since epoxy is insulating this is a clear issue towards fabricating working devices. In **Fig. 9(b,d,f)** a total of 4 min of plasma ashing is performed, The inset at the top shows how the lamella looks after the plasma ashing. The plasma ashing of 4 min. is a total ashing time consisting of two 1 min. ashings, followed by a single 2 min ashing. On the NC structure in **(a,b)** the surface roughness of the left-most NC exhibited relatively stable values of 1.11 nm, 1.06 nm, 1.09 nm and 1.13 nm, after each ashing step. The first value corresponds to an initial pre-ashing situation, and the final value corresponds to a total ashing time of 4 min. For the right-most NC the roughness values are less stable of 2.77 nm, 2.63 nm, 2.37, and 2.20 nm. Due to the continuously lowering of the surface roughness on one of the NCs there seems to be some removal of the residue. Since nothing much is going on for the partner NC positioned to the far-left of the same structure (see **(a,b)**), it could indicate that this NC does not have any residues on top of it. For the remaining two NC structures similar values are found. The second NC structure (**Fig. 9(c,d)**) exhibit roughness values on the left-most NC of 1.13 nm, 1.35 nm, 1.70 nm, and 1.44 nm. Similarly, for the right-most NC roughness values are found to be 2.41 nm, 2.01, 1.58 nm, and 1.37 nm, respectively for each ashing step. The third structure **(e,f)** exhibit roughness values for the left-most NC as 0.939 nm, 0.858 nm, 0.936 nm, and 0.802 nm. The right-most NC exhibit roughness for each step as 1.19 nm, 1.31 nm, 1.24 nm, and 1.36 nm.

Since stable surface roughness values are found in the vicinity of 1 nm, it could be that this is the surface roughness of InAs and not epoxy. Although, the AFM topography of the left-most NC of the third NC-structure with an average roughness of 0.88 $\pm$0.07 nm could be closer to the real InAs surface roughness, Compared to the NC in **(b)** both show stable values across different ashing steps, although the one in **(b)** exhibit values slightly higher of 1.1 $\pm$0.03 nm than the one in **(f)**. Currently it is not clear whether any of them has had all their potential residues removed.

It should be mentioned that after each ashing step, SEM images were acquired in order to follow the evolution as ashing proceeded. Although this data is not shown, SEM tend to alter the epoxy, perhaps through melting of it. This means that the data as discussed above should be taken with a grain of salt.

The showings here indicates that the epoxy is a real obstacle towards device fabrication. Having established an issue due to residues, in the next section, a similar investigation is employed, but this time without the influence of the SEM.

5.2 Plasma ashing of contaminated lamella

In the previous section, we encountered an issue of what appeared to be epoxy covering the surface of the NCs. The various degrees of such coverage was exemplified by the average surface roughness. For some of the NCs the values appeared to be stable after each plasma ashing step, however. AFM 3D maps indicated that InAs NC surfaces appear to be without residual epoxy when the surface roughness is below 1 nm. This is to some extend, backed by the SEM and AFM images of the NC which exhbited no contrast on its surface.

In this section, a systematic approach to increase reliability of residual indicators is employed. The NC will be subject of repeated AFM and plasma ashing steps; each step with a different plasma

ashing time, but without SEM micrograph, as it appears to contaminate the work.

A tendency arose while performing the repeated AFM and ashing steps. In **Fig. 10 (a,c)** two different NC-structures are shown in their original state just after being cut. Neither of these two NC-structures visually appear to be affected by epoxy coverage, but as previous section indicated, that does not need to be the case. The surface roughness on both of these NC-structures are similar: The NC in **(a)** appears to have a roughness of 1.23 nm, whereas the other NC in **(d)** has a roughness of 1.33 nm. These values are indeed similar to the NC-structures appearing to have epoxy on their surfaces, as shown in **Fig. 9**. As the process of repeatedly ashing the samples continued both NC exhibited yet again similar surface roughnesses, although steadily decreasing in contrast to the SEM and AFM probed NCs in the previous section. In comparison to the one NC in the previous section showing stable surface roughnesses below 1 nm, it took 26 minutes of plasma ashing, and is shown in **Fig. 10(b,d)**. The surface of both NCs appear considerably affected by the ashing, with a smoothened surface roughnesses of 0.910 nm and 0.886 nm, respectively. The insets show the extend to which the plasma ashing had on the lamella with local variations, in stark contrast to the one investigated in the previous section.

The hole in the epoxy next to the NC-structure in **(a,b)** is used to measured the height differences. Between the steps of as-sectioned NC-structure and 3 minutes of total plasma ashing. In this time frame, a total of 36 nm epoxy was estimated to be removed which indicated a plasma ashing rate of 9 nm/min. However, in the final 23 minutes of plasma ashing that took place between the 3 minute mark to the 26 minutes of ashing, only a mere 16 nm of epoxy was removed locally, bringing the total estimated epoxy removal up to ~ 52 nm with a severely decreased plasma ashing rate of 0.73 nm/min. Consult the Appendix for more data.

The resistance towards epoxy removal suggests a change to the sample preparation process is required. Comparing this lamella to the one in the previous section, indicates a dramatic change of epoxy properties. As described in the previous chapter, the sample preparation is mostly affected by the properties of the epoxy resin components. [51, 52] Possible reasons for varying properties of epoxy is aging of the components or contamination due to reaction with atmospheric moisture. The curing agent, which is taking part in the cross-linking during curing, readily reacts with water in a hydrolytic reaction, which breaks the chemical bonds, effectively decomposing the curing agent resulting in components of different properties.

5.3 Plasma ashing of non-contaminated lamella

The epoxy resin components used in this work has mainly been with components resulting in the varying behaviour as outlines in the previous sections. In order to properly examine whether the contamination indeed was an issue, the epoxy resin components were exchanged with new and fresh ones. Similarly to what has been done in this chapter until now, a systematic approach of AFM and ashing is employed in this chapter.

Figure 11 shows NWs cut into a NC structure with a skew cutting angle. In **(a)** a before plasma ashing AFM image of the NC structure is shown as it was cut. The mountain of epoxy right next to the structure is likely formed due to the skew cutting angle.

In **(b)** an after AFM topographic 3D representation of the plasma ashed structure is shown. The surface roughness of the NC before plasma ashing is 1.30 nm. This is similar to the values obtained in the two previous sections indicating a persistent need to remove residual epoxy on the surface. Plasma ashing for only a single minute yields a completely different surface roughness of 0.839 nm, which is on the order of previously stated data for NC assumed to have reduced its

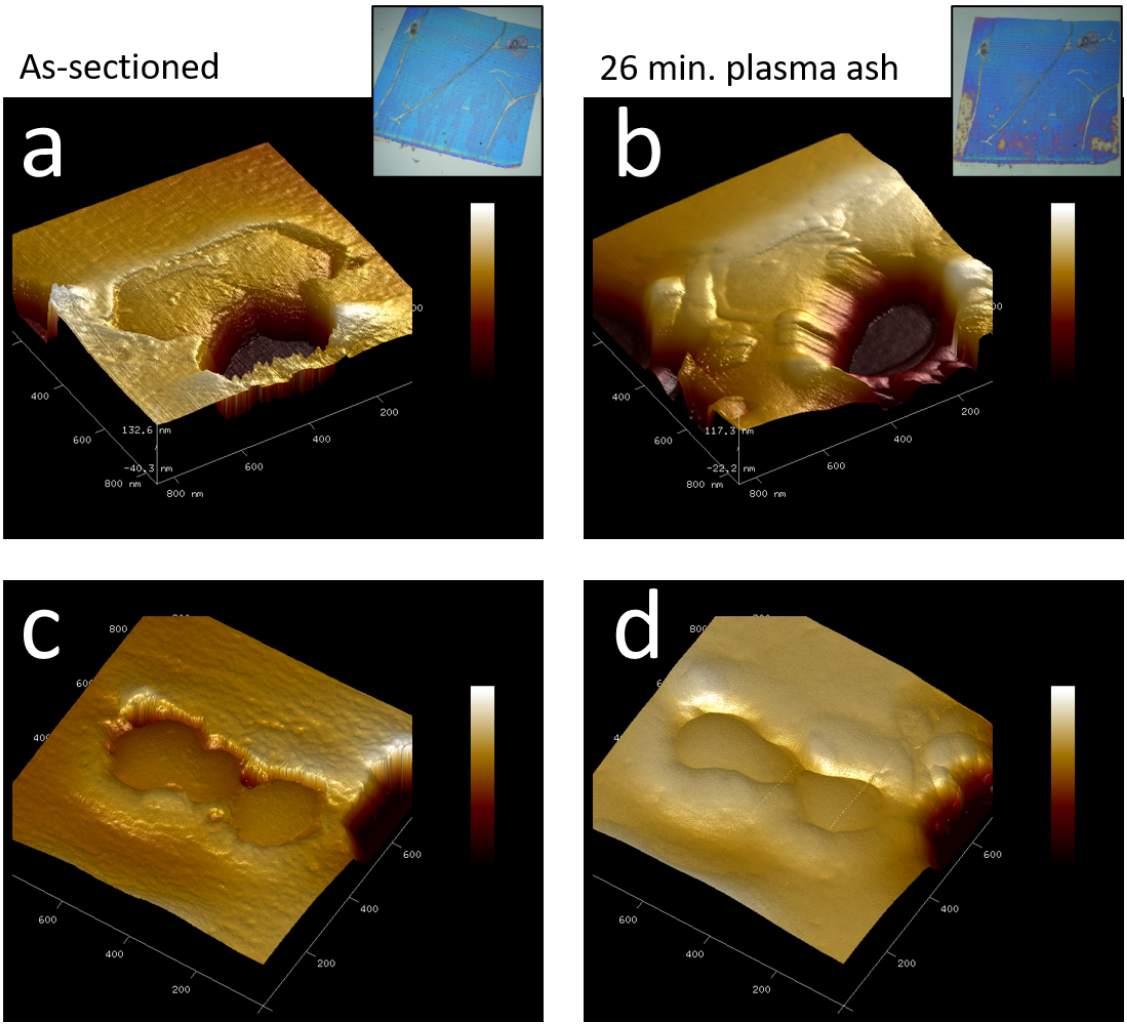

Fig. 10: Plasma ashing for 26 minutes. AFM topographical 3D representations are shown of two different NC structures (a,b) and (c,d), respectively. The structures in (a,c) are before any manipulations has occured, while in (b,d) the lamella containing the structures has been plasma ashed for a total of 26 minutes. The insets show the appearance of said lamella before and after being exposed to plasma ashing.

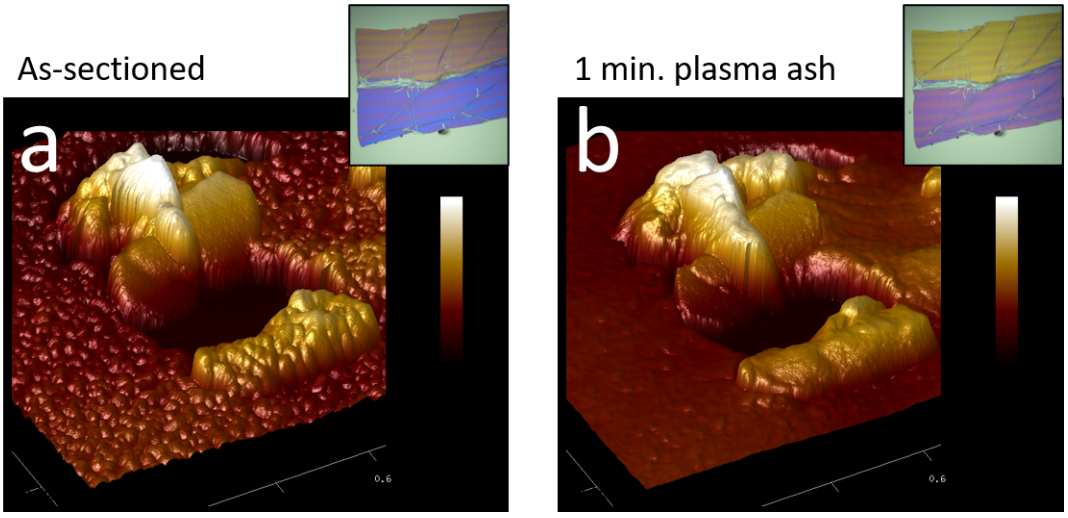

Fig. 11: Refreshed chemical components. (a) and (b) show AFM topographical 3D representations of the same Nc structure before and after being exposed to one minute of plasma ashing, respectively The insets show the appearance of the corresponding lamella before and after ashing, respectively

residual amount of epoxy on the surface. Previously, it took 26 minutes to attain surface roughness of that magnitude, but with the exchange of chemical components only a single minute seems to be required.

At present state the structure seems largely free of resin, except for the mountain of epoxy behind it. It is believed that this is likely due to the skew cutting angle, which also could explain the gaping hole next to the NC structure. Nevertheless, having a flat surface void of any obstacles as the epoxy mountain is paramount for successful device fabrication. In that regard, additional AFM and ashing was performed. **Figure 12** shows AFM topographical images of a lamella edge **(a-c)**, and of the epoxy lamella surface **(d-f)**. The images of both the lamella edge and the lamella surface are shown as they were sectioned, after one minute of plasma ashing, and finally after an additional three minutes of ashing, respectively. After having ashed for a single minute, 22.3 nm of epoxy appears to have been ashed away, and an additional 69.3 nm is ashed away after three minutes bringing the epoxy removal up to a total of 91.6 nm. A step height of 14.4 nm is measured at the edge, which means the total height at the edge is $\sim$ 116 nm. This is in good agreement with the set cutting thickness of 100 nm on the microtome in the sample preparation phase. The resultant plasma ashing rates is stable across both multiple ashing steps of 22.3 nm/min for the first minute, and 23.1 nm/min for the latter three minutes, which is in contrast to the rates obtained in the previous section.

The ashing of the epoxy surface showed an increasingly roughened and uneven surface with surface roughnesses of $\sim$ 1.1 nm, $\sim$ 2.5 nm, and $\sim$ 3.6 nm, for the initial state, after one minute of ashing, and after an additional 3 minutes of ashing, respectively. The magnitudes of the values are comparable with that of several of the NCs 1 nm. This indicates that at the beginning the NCs appear to have residual epoxy on their surfaces. Since the surface roughness on top of the NCs does not increase just like the epoxy surface, but reduces, it indicates that the plasma ashing is able to

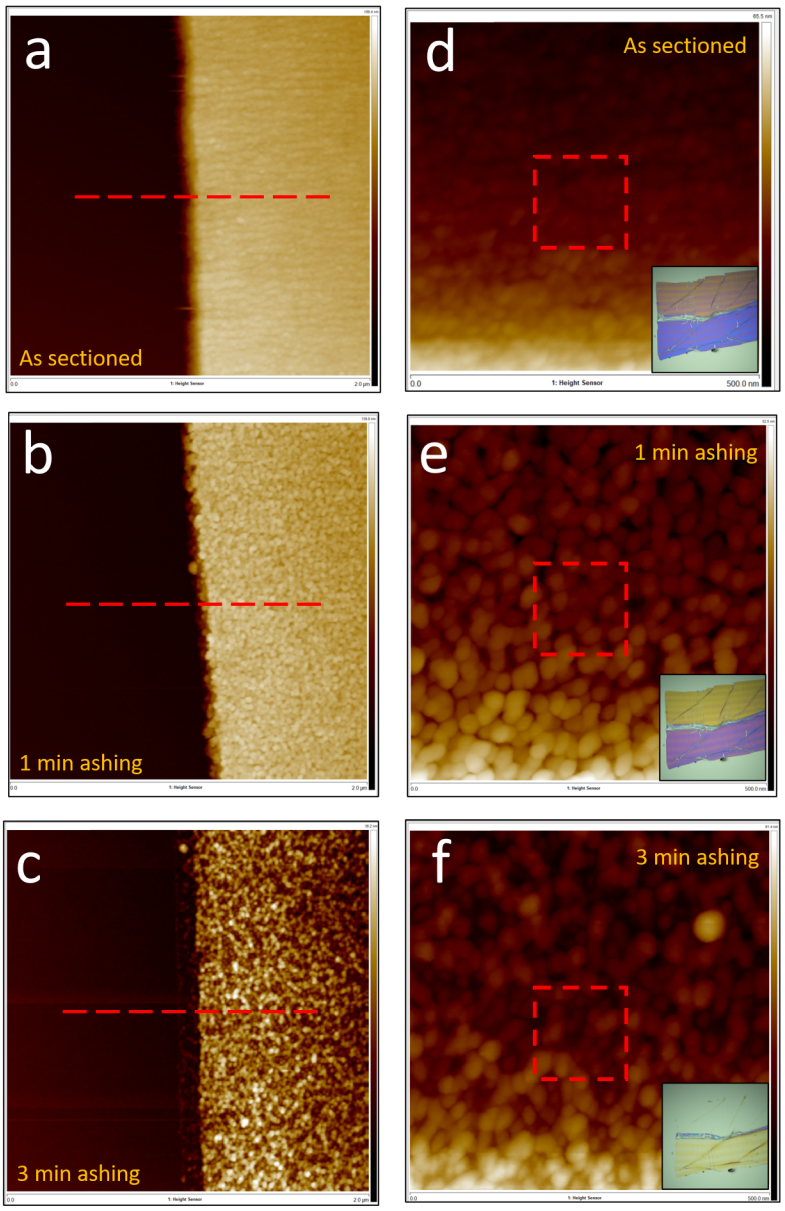

Fig. 12: Lamella step height and surface roughness. AFM topographical 2D representations of the lamella edge (a-c), and the lamella surface (d-f), respectively. In (a-c) the red dashed line indicates measurement of lamella step height after for each stage of the plasma ashing process. In (d-f) the red dashed box indicates surface roughness measurement.

remove the residual epoxy sitting on top of the NC structures.

In comparison with the work on the other epoxy samples, the exchange of aged chemical compounds with refreshed ones appears to have restored the properties of the epoxy. The improved ashing performance indicates a softer epoxy, and a prospect of increased reliability of device fabrication steps.

6 Fabrication on nanocrystals

In this chapter the general procedure of NC device fabrication is presented along with the limitations and obstacles that the generally small NC sizes can contribute with. Not all obstacles that proves problematic for fabrication has been fully accounted for or eliminated. Most of the device fabrication in this work was done using the aged epoxy resin chemicals, as discussed in the previous section, and as such has suffered accordingly.

The remaining issue at present is slightly misaligned electrodes. In contrast to a traditional NW with a long dimension, the smaller sizes of NC structures limits the area to make proper contact between the electrodes and InAs, and consequently also limits the space for gate electrodes. A possible reason for misalignment can be due to beam deflection of the electron beam in the Elionix 7000 during electron beam lithography (EBL) within a single write field. The difficulty of placing the lamella exactly at the center of the Si substrate for devices makes the beam deflection a contender for the misalignment.

6.1 General procedure

The general procedure to fabricate consists of several steps as shown in **Fig. 13**. The first step after having transferred the lamella is to form an electron beam defined mask. This is done by by depositing electron beam resist, PMMA AL6, next is to spin the substrate to evenly distribute the resist, followed by a hardening step. After the resist has hardened, the desired pattern is exposed onto the resist by EBL forming the mask pattern. A subsequent step of development is required to remove the exposed areas, resulting in a mask protecting the substrate where metal is not supposed to be deposited. Finally, metal is deposited followed by the removal of the mask, known as lift off.

6.2 A detailed account of fabrication steps for nanocrystal devices

The very first step of fabrication is to inspect and identify potential NC candidates by scanning tunneling microscopy (SEM) after the lamella has been transferred to the chip substrate. The Raith eLine is an SEM, which enables automated captures of the NCs, limiting the exposure of the NCs to a minimum. [18, 17]

Figure 14 gives an example of the SEM obtained from the eLine, where a close-up of the NC of interest is highlighted by a dashed blue box, and the rest of the images being potential candidates found in the lamella as well. The small alignment mark crosses in each corner of the image have four arms each of 500 nm in length, and are a necessity to accurately position the electrodes correctly upon electrode designing. The crosses are fabricated much in the same way as devices are, except they are limited to 100 nm of Au, while RF milling is not necessary. The minimization of exposure limits the resolution of each image, and in combination of the small NC structures on the order of $\sim$ 450 nm can prove an obstacle when determining whether the individual NCs are too far away

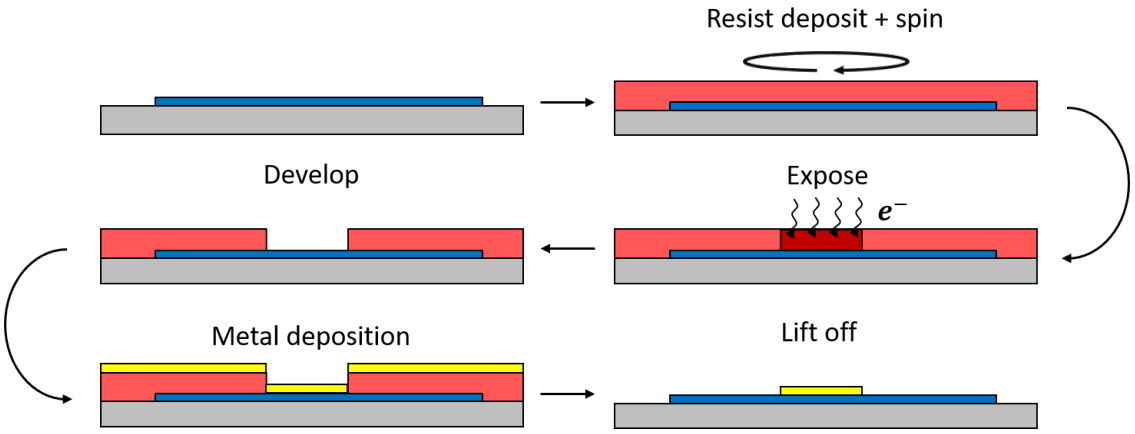

Fig. 13: General cleanroom fabrication. The fabrication process entails depositing resist (red) on top of the substrate containing the lamella (blue). Following is spinning of the resist, after which the hardened resist is exposed by an electron beam to define the pattern. The exposed areas are dissolved by development, followed by metal deposition, and finally ending in lift off

from each other. Once the NC structure candidates are found, the electrode design process follows, and the resist mask can be created.

The mask creation begins with spincoating the substrate with a single drop of PMMA deposited. This is likely to decreases the risk of dried resist on the side and beneath the substrate. The spinning is done at 4000 rpm for 60 seconds, and subsequently hardened by vacuum for one hour. As a consequence of the various issues of the lamella, the effect of softbaking the electron beam resist at 185 °C is not fully understood, as will become clearer in section 6.3.

A drawback of the lamella transferring process is the likelihood of contamination. As the sectioning process can be long-lasting, the water in the knife-trough is likely to be contaminated by e.g. grains of dust. Unfortunately it is illadviced to clean the sample by means of MQ and/or IPA with a subsequent drying by N2, as the sample appears to suffer by wrinkling. See the Appendix for such an example. The impurities are likely to be removed after the lift off process, but if sufficiently large streaks in the spincoated PMMA will appear, and will consequently distort the height locally.

Once the PMMA has hardened, exposing it to an electron beam by EBL imprints the design pattern by chemically altering the PMMA. The exposed pattern in the PMMA is then dissolved by dipping the substrate into a solution of 1:3 MIBK:IPA for 60 seconds followed by 30 seconds of IPA. The sample is dried by N2-air flow.

The manipulaiton of the InAs surface result in contamination of different kinds. Due to being embedded in an epoxy matrix and having deposited resist, residuals of those materials can be present after development. Additionaly, since InAs forms a native oxide layer where the interface is believed to have a high density of defects that degrades its electronic properties.[40] The organic materials are removed by means of oxygen plasma ashing. However, as discussed in the previous section 5, the epoxy had removal issues. Hence, the devices fabricated in this work has been of varying ashing times; of 30 seconds, one minute and two minutes.

Although the device functionality remains elusive, the exchange of chemical components with fresh ones, significantly reduced required ashing time to remove excess epoxy. For least possible

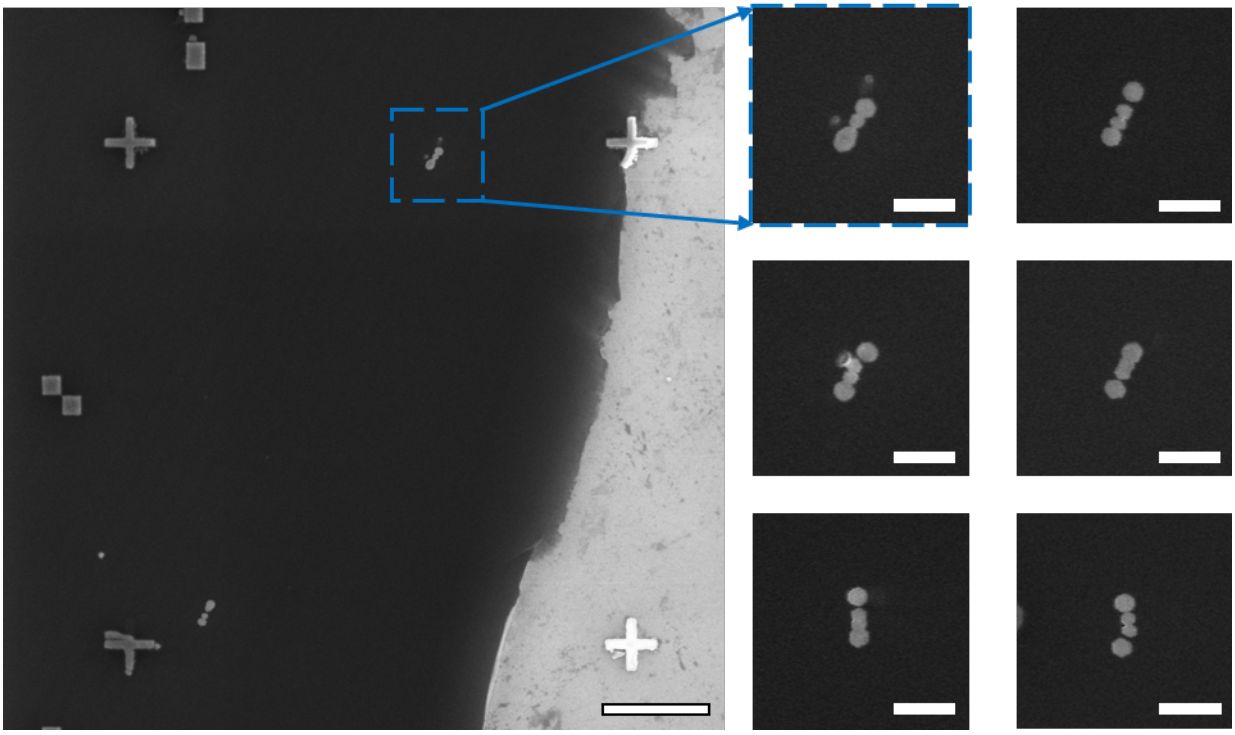

Fig. 14: The large-scale image is an automated SEM example showing a candidate for fabrication in the blue, dashed box. Other candidates are shown as well, each of three NCs conjoined to some extend. Scale bar for the large image is 2 μm whereas for the close-ups of several NC structure candidates the scale bar is 500 nm.

manipulation of the InAs surface, plasma etching should be limited to being as short as possible. Increased ashing times has been shown to damage the sample by oxidization, which proves to be detrimental for device performance.[53]

After the substrate has been ashed, it is loaded in a physical vapor deposition system, where the surface cleaning of the native oxide is performed by RF ion milling with Ar flow for 8 minutes at 15 W. Subsequently, 5 nm of Ti and then 200 nm of Au is evaporated to onto the substrate. The necessity for a layer of Ti is in order to stick the Au onto the chip.

Following metal deposition, the excess resist is removed by warm acetone at 50 °C, leaving only the regions of Ti/Au in physical contact with the substrate surface behind, as seen in **Fig. 15**. Two different sets of devices are shown in **(a,b)**, with corresponding close-ups in **(c,d)**. In **(c)** the close-up shows broken Ti/Au leads due to the sudden change of height due to wrinkles or folds in the lamella. The thicknesses of the leads are 1 μm. The same reasoning is applied for the lamella edge. The leads, as the ones shown in **(d)**, are designed to be 2 μm wide across the edges, and will usually remain intact. To aid the process of lift off, a pipette can be used to create a steady stream of the warm acetone.

6.3 The effect of heating an epoxy lamella

The lack of reproducibility of device fabrication meant that the the unknown effect of heating the lamella during spincoating was investigated. The steps taken to understand how the lamella responds to heating are similar to the steps when the effect plasma ashing was investigated (see section 5), consisting of AFM surface topography imaging in-between each heating exposure of the lamella. The heating is done on a hot plate at 185 °C for one minute, matching the softbaking procedure of resist hardening for the first heating test, and two minutes for the second heating test. The AFM surface probing was done at different areas of the lamella, each for their own purpose: The corner of a lamella was scanned due to it being easy to find on separate occasions. Here the lamella height can be observed. The lamella surface is also probed in order to get surface roughness estimates of the epoxy surface, and finally a NC structure is scanned so the effect of lamella heating can be observed in in vicinity of NC structures. To be able to compare surface roughnesses the area of extracted values was kept to $\sim 100 \times 100$ nm. This is also the area used for surface roughnesses in section 5.

The lamella-to-Si-substrate height differences for the three cases of as-sectioned lamella, 1st heating, and the 2nd heating are extracted as indicated in **Fig. 16 (a-c)** by the dashed blue lines. The height differences between the Si substrate and the epoxy surface Δh_{Si} changed after heating for one minute at 185 °C from 57.4 nm to 47.1 nm, but nothing much happened for the next two minutes of heating, resulting in a height difference of 48 nm.

As for the lamella surface, as shown in **(d-f)**, the unmodified, as-sectioned lamella showed a decrease of average surface roughness $R_a^{lamella}$ from 1.1 nm to 0.33 nm, which was followed by an increase of roughness after the subsequent two minutes of heating to be 0.81 nm. Nevertheless, in order for these values to mean anything, comparison of the values with extracted ones for the NC structure is necessary. In **Fig. 17** two cross-sectioned NWs appear with a skew surface due to misaligning of the diamond knife of the microtome. In **(a)** all of the surfaces appear relatively rough, whereas for the 1st heating test **(b)** it appear smoother, followed by a slight roughening after the 2nd heating **(c)** (i.e. an additional two minutes of heating). Just like what was observed at the corner of the lamella, there appear to be a height reduction after the 1st heating Δh_{NC}, as the height difference between the lamella surface and the NC is 19.4 nm being reduced to 15.6. The

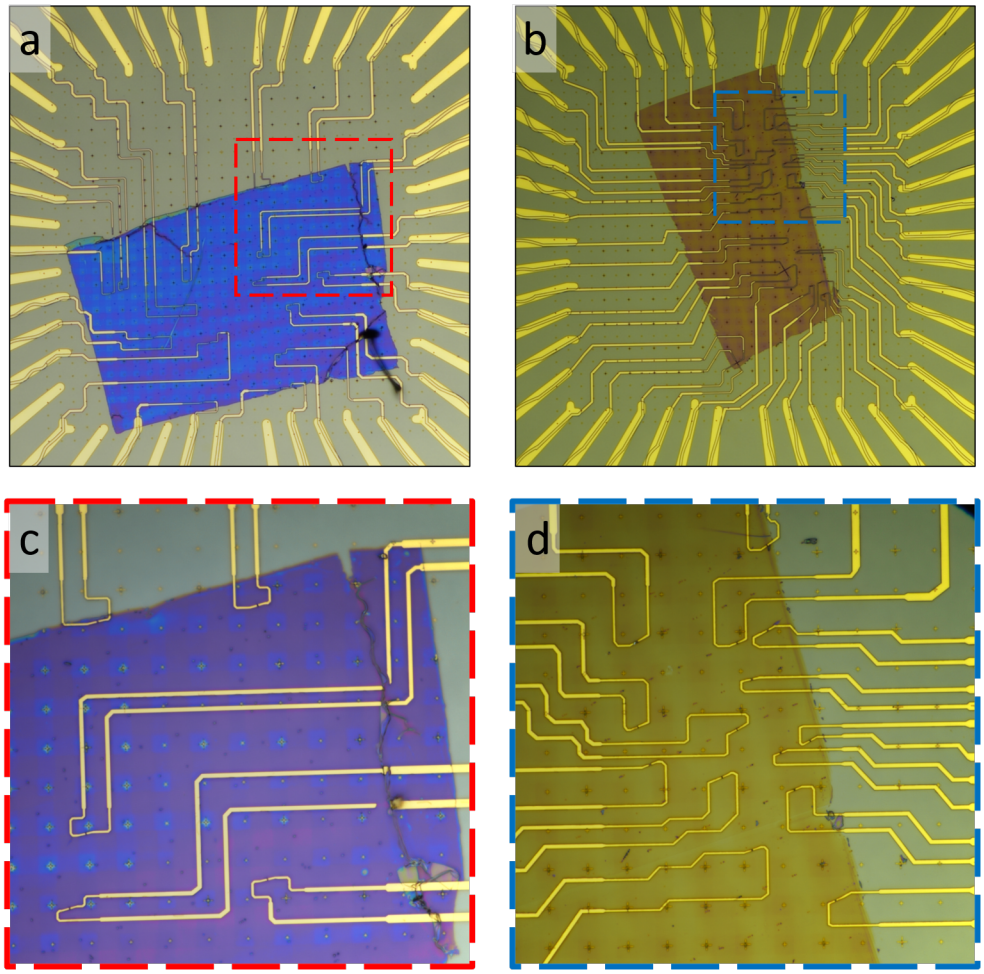

Fig. 15: Lift-off. In (a,b) are shown optical images of two different device sets, respectively. The dashed squares corresponds to magnified optical images of the enclosed areas (c,d). No scale bar is present due to the optical microscopes inability to measure properly.

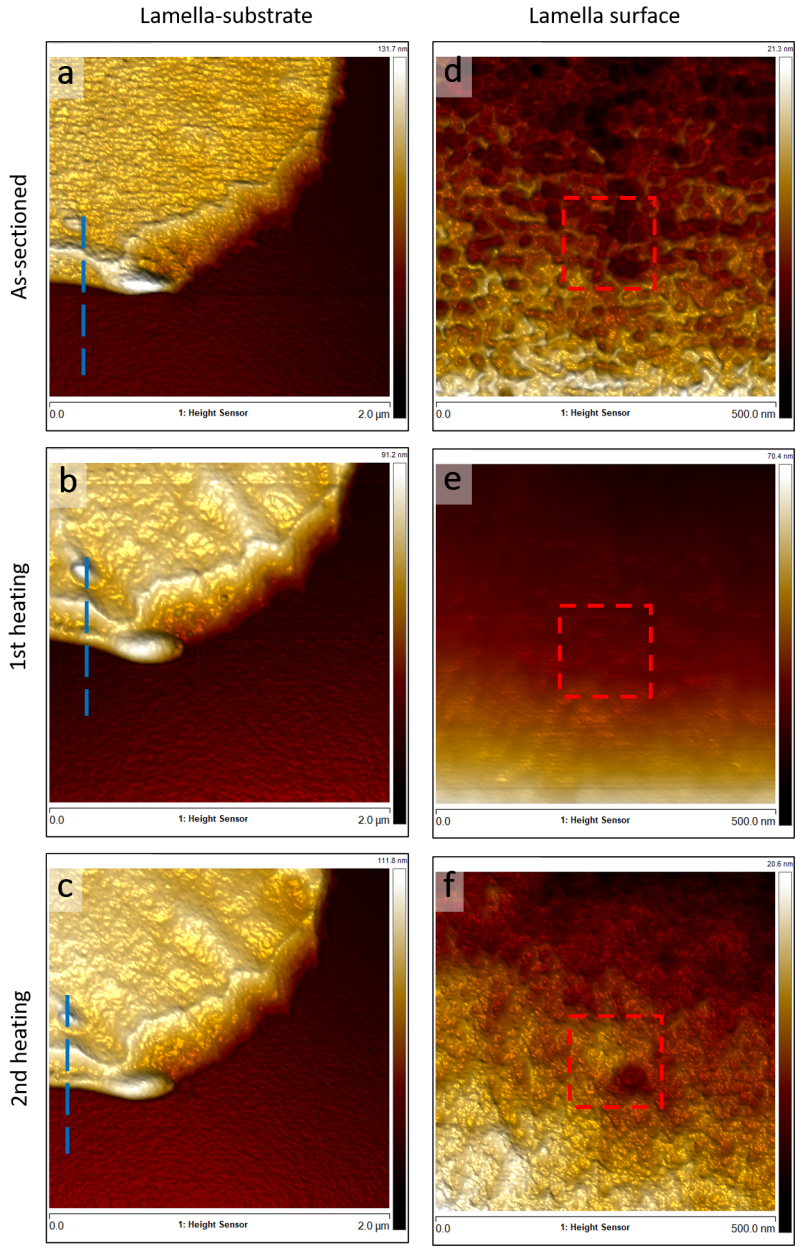

Fig. 16: Heating of lamella. In (a-c) the heating effect is seen by means of AFM of a lamella corner, where the blue, dashed line represents where vertical distances were examined between the lamella and the Si substrate. In (a,d) not modulation of the lamella is applied, in (b,e) 1 minute of 185 °C, and (c,f) for 2 minutes of 185 °C. Consequently, in (d-f) the surface roughness is calculated on the lamella surface, as indicated bu the red, dashed square.

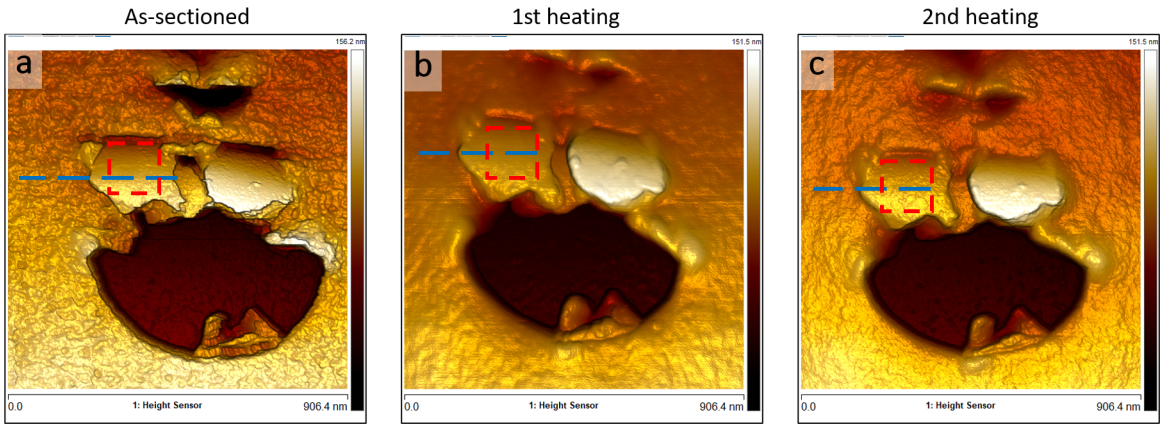

Fig. 17: Surface roughness and step height of NC. In (a-c) the surface roughness is measured as indicated by the dashed, red square, and the vertical height is measured between the lamella surface and the NC, as indicated by the blue, dashed line. This is done before manipulating the sample (a), after 1 min of 185 °C (b), and after 2 min of 185 °C (c).

subsequent heating showed a similar value as before of 16.5 nm. Just like for the lamella-substrate height difference, there appear to be little variation after the 2nd heating.

The surface roughness of the NC R_a^{NC}, as indicated by the dashed, red boxes on top of the NC for each heating step **a-c**, respectively. Initially before modifying the lamella surface, the surface roughness is 1,1 nm, where it reduces to $\sim$ 71 nm after 1 min. of heating **(b)**, and slightly increases after yet another 2 min. of heating **(c)** of $\sim$ 0.84 nm.

A summary of these values can be found in table 1. It appears that the height of the epoxy lamella only changes substantially after the 1st heating, whereas it appears more-or-less constant after the 2nd heating.

Since epoxy is an amorphous thermosetting polymer, it remains rigid up until a certain temperature, namely the glass transition temperature. Typically for epoxies, the transition temperature is in the range of 150-265 °C. Beyond this temperature the polymer network begins to relax, and the epoxy becomes softer.[39] In contrast, the electron beam resist, PMMA, is a thermoplastic polymer with a glass transition temperature on the order of 105 °C. [48] The reduced epoxy lamella thickness is similar to what happens for PMMA during heating, namely a reduction of thickness. The reduction for PMMA is due to evaporation of solvents, which consequently increases its mechanical strength. Since both exhibit thickness reduction at an applied temperature of 185 °C, which *can* be above the glass transition temperature for both of them, it is possible that the epoxy experiences similar evaporation of excess solvents. No apparent widening of the lamella is observed, which would otherwise indicate that the epoxy would be melting rather than having its excess solvents evaporating.

In **Fig. 18** the NC structure as previously discussed in section 5, is shown here after ashing for a total of 26 min. **(a)**, and a subsequent heating for five min. at 185 °. The NC surface roughnesses of this NC structure are obtained in the areas of the dashed boxes. In **(a)** the surface roughness is 0.89 nm, in **(b)** the surface roughness is 0.70 nm. In comparison, the surface roughness of the NC investigated in **Fig. 17** is also $R_a^{NC} = 0.71$ nm after the 1st heating. In line with the discussion

	As-sectioned	1st heating	2nd heating
Δh_{NC} [nm]	19.4	15.6	16.5
Δh_{Si} [nm]	57.4	47.1	48.0
$R_a^{lamella}$ [nm]	1.1	0.33	0.81
R_a^{NC} [nm]	1.1	0.71	0.84

Table 1: Summary of heating test. The data is separated into three categories: As-sectioned, 1st heating, and 2nd heating, respectively. As-sectioned is the unmodified lamella, where 1st and 2nd heatings are the lamella subjected to one and two minutes of 185 ° on separate occasions. The three categories are displayed with values for height differences of between a NC and the surrounding lamella surface Δh_{NC}, and for the height differences between the Si substrate and the lamella edge Δh_{Si}. The lamella $R_a^{lamella}$ and NC R_a^{NC} surface roughnesses are also displayed, respectively.

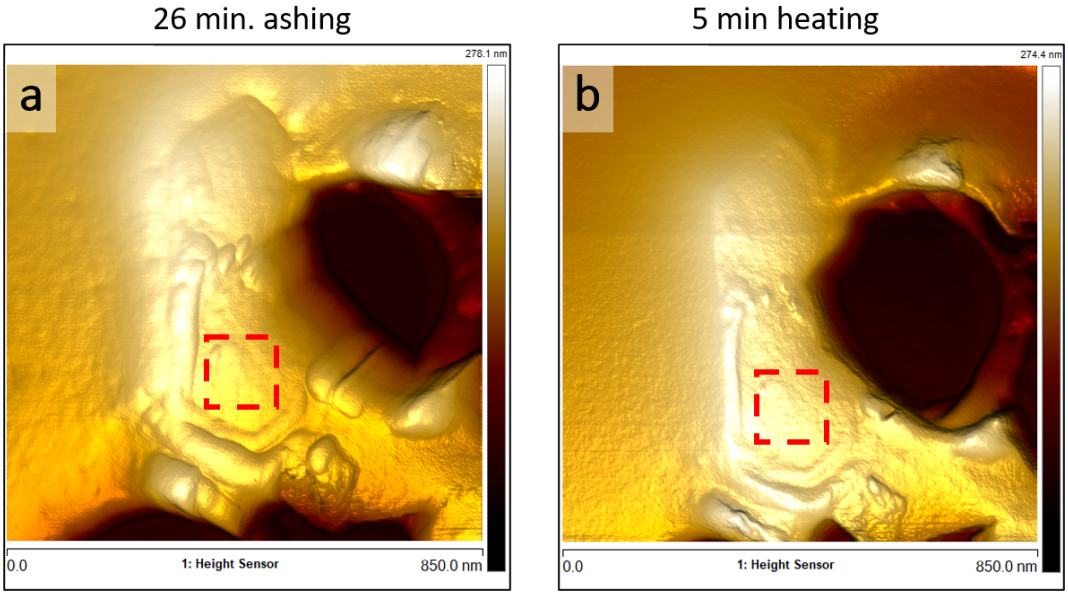

Fig. 18: Heating on contaminated lamella. In (a) an extremely processed NC structure with a total of 26 min. of plasma ashing. In (b) the very same NC structure is heated for 5 min. at 185 °C. Surface roughnesses are obtained in each case at the red, dashed square.

about evaporation of excess solvents in the epoxy, the reduction of surface roughness in both of these two cases could indicate even further removal of residual epoxy after heating. However, if this indeed is the mechanism of epoxy subject to heating, then it is also expected that the mechanical strength of the epoxy increases as well, due to the polymer chains packing even tighter than before solvent evaporation.

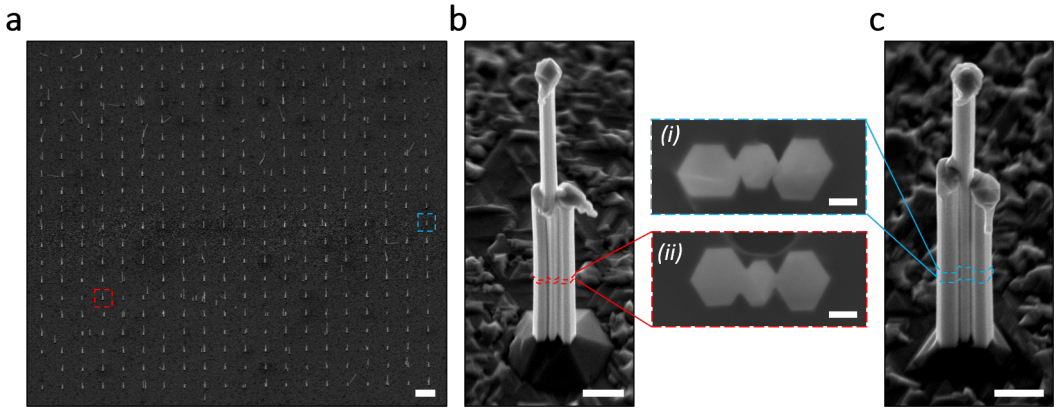

Fig. 19: Cross-sectioning InAs nanowires. In (a) an SEM micrograph representing a typical NW array. The red, dashed square and the blue, dashed square represent the NW depicted in (b) and (c), respectively. The panels *(i)* and *(ii)* represents CS NWs of their parent NW system. The dashed lines in (b) and (c) represents the approximate position of cutting; about 600 nm above base. The scale bar in (a) is 10 μm, and for (b,c) is 500 nm, while the panels have scale bars of 100 nm.

7 Three conjoined InAs nanowires for cross-sections

The InAs NWs are grown on InAs ⟨111⟩B substrates using the vapor-liquid-solid mechanism. The substrates are pre-patterned using electron beam lithography, and grown with Au seeded particles as catalysts. The growth process was performed by Thomas Kanne.

In **Fig. 19** we show an SEM micrographs of a typical 20 × 20 NW array **(a)**, with example NWs highlighted in the dashed, color-coded squares, which are enlarged in **(b,c)**. By keeping track of the position of the NWs in their array, and subsequently in the sectioned lamella, it is possible to relate the cross-sectioned NWs to their parent state of standing NWs. This is indicated by the color-coded panels *(i)* and *(ii)*, showing their approximate positions of where they were cut from during the microtomy phase, respectively. Each NW is cut about 600 nm above base level. The figure provides an ideal situation of three wires connected in series in a corner-to-corner fashion, which is illustrated in the panels *(i)* and *(ii)*. The SEM images are taken with 30

As is usually the case when it comes to investigating NWs using electron microscopy techniques and fabricating devices, one can investigate the NW surface using an SEM before and after device fabrication. In addition an in-depth investigation of the crystal structure itself using the TEM is limited to be of a different NW.

III-V semiconductor NWs commonly include defects such as stacking faults, twins, and polytypism due to the crystal phase alternating between zinc-blende (ZB) and wurtzite (WZ). Such crystal structure differences can affect device properties by modifying the electronic band structure[34] or by incorporating scattering centers for electrons.[46] Hence, imperfections or variations in crystal structure appear to have implications on device properties.

By virtue of the crystallinity and the electron transport relationship it is important to be able to properly characterize the NWs used for devices. With this in mind, cross-sectioned NWs have

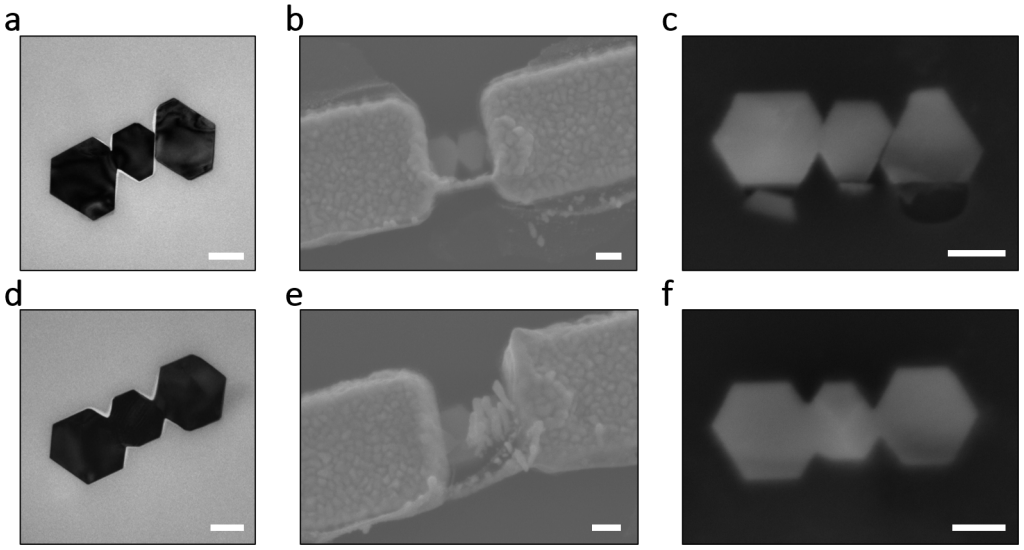

Fig. 20: Successive lamellae transfers. (a-c) and (d-f) are both cases of NC structures cut from the same NW located across successively sectioned lamellae. (a,d), (b,e) and (c,f) are lamellae transferred to a TEM grid, device substrate, and a Si substrate, respectively. Scale bars are 100 nm.

the advantage of being able to do so by transferring subsequent sectioned lamellae to various substrates. See **Fig. 20**. The example of such a work-flow provided in the figure, consists of three different lamellae cut during the same microtome session, obtained in quick succession. In each row, the cross-sectioned NWs originating from the same free-standing NW are located. The first sectioned lamella was transferred to a TEM carbon-coated copper grid (**(a)** and **(d)**). The following sectioned lamella was transferred to a highly-doped Si substrate with 200 nm SiO_2 (**(b)** and **(e)**), and finally the third sectioned was transferred to a Si substrate for SEM characterization (**(c)** and **(f)**). Measures was taken to make sure the CS in **(c)** was correctly identified, which could indicate the wires fracturing. Each lamella was cut with a ~ 100 nm thickness with a speed of 1.6 mm/s. For various reasons, such as unfortunate placement of sections on the TEM grid, folds or wrinkles in the lamella arising from transferring are all risks severely limiting the attainability of locating the correct CS NWs across different lamellae. In addition, as would be the case for this example concept, the devices fabricated had issues of Au bridges across the two leads resulting in shorts. As illustrated in the figure, successful transfers of one lamella after the other to three different substrates, each with a different purpose, enables various characterizational opportunities on the same NW.

7.2 Transmission Electron Microscopy of a Single InAs Nanocrystal

This section will be to provide a reference CS NW for the section that follows 7.3, where the crystal structure of the constellation of three conjoined InAs NCs are investigated.

Hence, an in-depth look into the crystal structure of a single InAs NC will take place in this

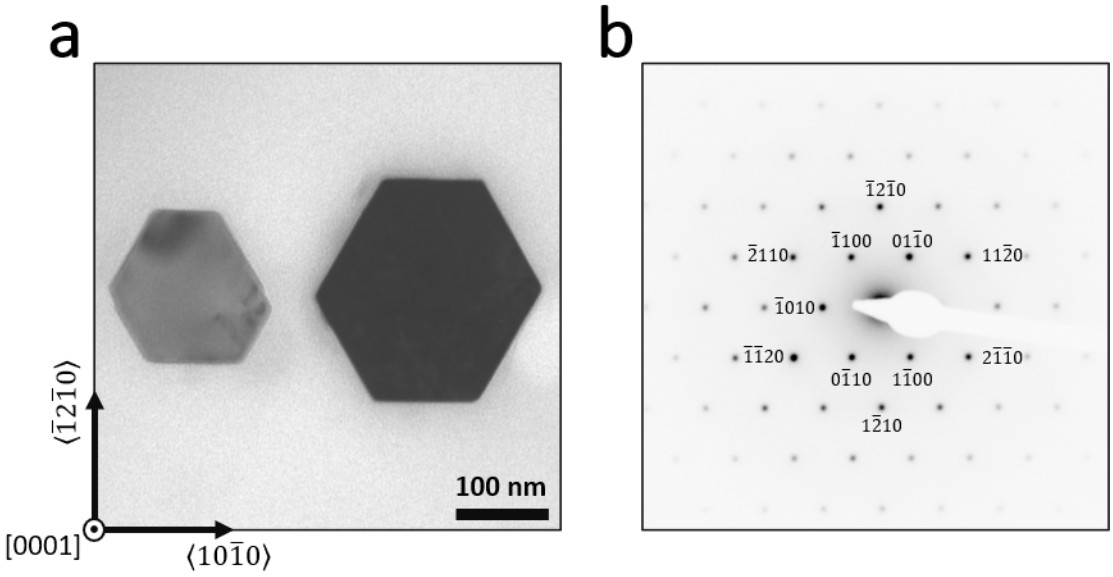

Fig. 21: A single InAs NC. In (a) is shown a TEM bright-field micrograph of an InAs NC aligned to its high-symmetry axis [0001]. In (b) is shown its corresponding diffraction pattern with the crystallographic planes labeled.

section, in order to compare it with the observed variations of the three conjoined NCs.

The NC-systems in this section and the next deals with NCs originating from the same sectioned lamella. This means despite any local variations during growth, all of the NC in the lamella should be grown under identical conditions. In this way, this single InAs NC which is going to be discussed shortly, could prove to be a good reference point in comparison to the appearance of the three InAs NCs in serial connection.

We will start our analysis by looking at a single NC using the TEM, as seen in **Fig. 21**. The figure is a birght field (BF) micrograph **(a)** shows a large NC pictured alongside a smaller one. The large NC measures ≈ 244 nm from facet to facet, and ≈ 247 nm from corner to corner, and is aligned to its high symmetry zone axis WZ[0001], as is seen in the selected area electron diffraction (SAED) pattern micrograph **(b)**, i.e. the growth axis. The pattern is displayed in reciprocal space, and is the manifestation of the crystal lattice in real space, resulting in a distinct pattern of a close packed hexagonal (CPH) crystal lattice. Each of the closest spots to the direct beam, situated in the center, in the SAED pattern is labeled with their relative spots. The inner spots are of the $1\bar{1}00$ family of planes with corresponding $\langle 1\bar{1}00\rangle$ reciprocal lattice direction. They point towards the corners of the NC in real space, while the $\bar{1}2\bar{1}0$ family of planes make up the facets of it.

An analysis of the SAED pattern of the two inner-most family of planes reveal that the relative distances from the direct beam to $1\bar{1}00$ is on average 0.615 ± 0.0023, while the distance to the $\bar{1}2\bar{1}0$ planes on average is 1.067 ± 0.0025. However, using ImageJ[13], a scientific image analysis software,

there is an uncertainty revolving the way of obtaining these values, considering that the most simple way of measuring distances as well as angles is by selectively choosing points or pixels of interest. The method is elaborated in the Appendix, but in short it is a two-step process of carefully tracing a line between two spots of the same family of planes sitting opposite each other, and plotting said trace, where the distance between the centres of peak intensity is measured. Since the images has a specific resolution and consists of 2048×2048 pixels, the accuracy of each step can be rather limited. By following the procedure, as explained in more detail in the appendix, approximate uncertainties of each step has been extracted and combined through combination of errors[2] to be 0.0021, which is comparable to the standard deviation of either of the averaged reciprocal distances $1\bar{1}00$ or $\bar{1}2\bar{1}0$.

The relative angles of each set of family of planes are measured to be $60.0° \pm 0.18°$, and $60.1° \pm 0.22°$. The data extraction can be found in Appendix. Following the same argument of manually selecting points of interests, as above for measuring distances, there is also an uncertainty when it comes down to measuring the relative angles of different lattice planes. The uncertainty associated with the choice of pixel is 0.21°, which is similar to the standard deviations of the averaged angles. The process of measuring angles and the extracted uncertainty is found in the Appendix.

In relation to the deviations of either relative angles or reciprocal lattice distances, the extracted uncertainties imply a well-defined crystal lattice very close to, if not exactly, a textbook example of either a cubic or a CPH crystal lattice[11]. Although, the sample size is limited to a single example of an isolated NC, it does indicate that the lateral stress[55] applied to the crystal during mechanical cutting of the standing NWs using the Microtome does not sufficiently affect the crystal lattice. Other studies using mechanical force to bend NWs has shown to significantly alter the crystal by introducing defects such as dislocations, and eventually grain boundary formation consisting of chaotically arranged lattice planes[54]. In that regard, this NC exhibit no clear signs of defects nor of stress fields which could otherwise dramatically affect its properties in use for quantum devices.[57, 38]

In the following sections, this particular NC will serve as a reference for slightly more complicated structures consisting of three NCs in series merged into a single large structure.

7.3 Three InAs Nanocrystals in Serial Connection

In the previous section 7.2 we introduced the singular InAs NC exhibiting an exemplary SAED pattern aligned to the high symmetry zone axis of WZ[0001]. In this section we take a look into the characteristics of three InAs NWs pre-patterned by EBL to be positioned so close to each other that they form a larger structure of three NCs in series. The singular NC will serve as a reference to the three combined NCs. All data shown in this section, along with the singular NC, stem from the same lamella. Hence, the NWs are all grown under identical conditions, and cut into sections under identical conditions.

Despite the entire process has been identical for all NWs, they do exhibit various shapes and sizes, as seen in **Fig. 22**, as well as different extend of merging of NCs. Still, some of them share some traits. **(a,d)** are cases of similar shaped NCs where only two of them are merged with the third NC situated such the facets are parallel to each other, and in close proximity. **(b,c)** are both cases of the middle NC merging with the two others through the corners to a certain degree, while **(b)** exhibits more symmetrical hexagonal structure of each NC. The last two, shown in **(e,f)**, are cases of structures with NCs merged to a much larger extend than the others.

All of the TEM micrographs are aligned to the high symmetry zone axis [0001] of the middle NC. The varying shapes are likely due to local fluctuations of the growth kinetics resulting in varying

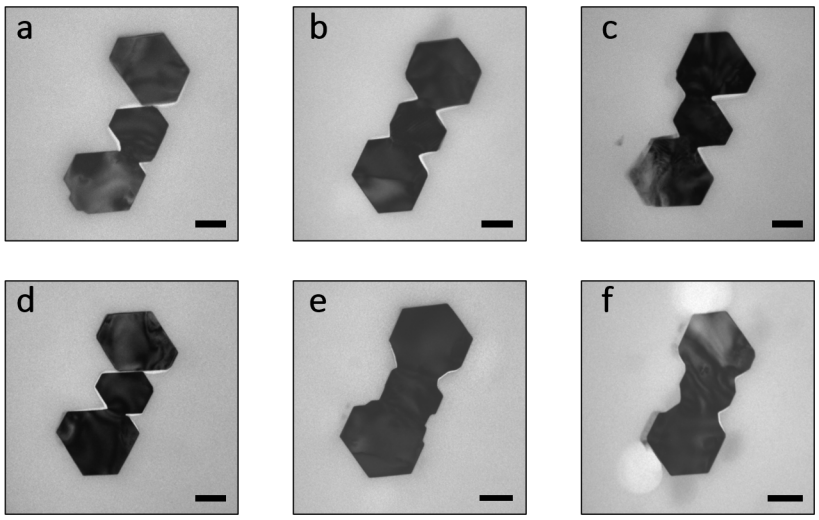

Fig. 22: Three InAs nanocrystals in series. Each individual NC-structure vary in some sense in regards to sizes, and extend of merging of multiple NCs. (a,d) only consist of two merged NC, while (b,c) appear to mainly connect at their corners, and (e,f) exhibit a much larger extend of individual NC merging. These structures are subject to crystal lattice analysis by means of their respective SAED patterns. Scale bars are 100 nm

$11\bar{2}0$ facet sizes[5], and perhaps slightly varying Au seed particles.

Compared to the NC discussed in section 7.2 (**Fig. 21**) all of these in **Fig. 22** exhibit contrast variations. Plenty of work has previously been done on various kinds of complex structures such as core-shell heterostructures[7] and semiconductor-superconductor hybrids[22]. Mutual for these structures is, a combination of different materials result in strain at the interface due to lattice mismatch of the applied materials, which can potentially induce dislocations in order to relieve the strain.

Hence, it would not be surprising for two or more NWs growing in close proximity to each other to attain strain at the interfaces. In principle, smaller NWs tend to possess more efficient strain relaxation than larger ones, and *G. Stan et al* has shown that there is an inverse relationship between NW radius and the elastic modulus[45]. The cross-sectioned NWs (**Fig. 22**) are on the order of 150-250 nm in diameter, which is considerably larger than then ones reported in ref. [45]. Although they report on ZnO NWs, at diameters of $\sim$ 120 nm the obtained values of elastic modulus approached that of the bulk value.

Nevertheless, it does not change the tendency that the larger the diameter of a NW, the smaller the elastic modulus of the material is. This is to say, that less stress is required in order to displace material particles. Thus, the varying contrast as seen in the figure, could indicate bending contours as a consequence of the mechanical force applied during the sectioning[54],[42], or be a result of the individual crystal lattice bending due to the introduction of dislocations[16].

High-resolution TEM (HRTEM) or even high angle annular dark field scanning tunneling electron microscopy (HAADF-STEM) would be the ideal way to probe such imperfections in the crystal lattice, where dislocations could be readily observed, and the interplanar distances extracted for

various planes. Since no such data will be presented here, there will be no clear signatures of any defects in the crystal. Yet, in an attempt to give an estimate for such behaviour of the NC crystal structures, a SAED pattern analysis is performed.

The reciprocal space is a Fourier transform of the predominant crystal structure, which means if the part of the NW that has been locally sliced into a NC contains a high enough density of imperfections then it would be observable in the TEM BF micrographs and their corresponding SAED patterns. Considering the SAED pattern shows Bragg diffracted electron waves, which can be related to the real relative positions of the direct atomic lattice, it would not be a surprise if stress-induced displacements of the crystal lattice would manifest a corresponding SAED pattern mimicking just that. The contrasts on each NC for the various NC-geometries (**Fig. 22**) indicates imperfections in the crystal lattice, and as already noticed, the single NC as discussed in the previous section 7.2, did not exhibit any strong intensity variations of the NC, and did exhibit an example of a CPH crystal, all the while being cut under identical conditions as the ones in **Fig. 22**.

Although the varying contrast in each NC (some more than others) could be indicators of grain boundary formations[54], especially at the merging of two NCs (**Fig. 22 (a-d)**, some appear vague and difficult to observe. In order to enhance the visibility of imperfections in the crystals, the TEM was operated in dark-field (DF) mode, where a specific Bragg diffracted SAED spot is chosen and isolated to visualize the planes responsible of the particular SAED spot. Such investigation were performed on three of the displayed NC-structures in **Fig. 22 (b-d)**, and is shown in **Fig. 23** of various SAED spots. Each column of the figure **(a-c, d-f, g-i)** correspond to a specific NC-structure, each with the middle NC aligned to the high-symmetry zone axis of WS[0001], but of varied SAED spot of interest. The insets are graphics reflecting the SAED pattern of the middle NC, where the white spot indicates the specific plane that is isolated to perform and execute the DF micrographs. The specific plane is also indicated with its Miller indices and displayed in the center of the inset.

The white intensity correspond to the diffracted electrons, and considering that they all appear disorganized they work as indicators, just as in the cases of the BF micrographs, of bent crystal lattices. However, **(d-e)** appear much more disorganized than **(g-i)** and **(a-c)**, of which it can be discussed is more or less impacted by impurities in the lattice. The plane $< 10\bar{1} >$ **(f)** of the middle column, which is the crystallographic orientation of the corners used to merge the NCs, appears highly distorted in the two outer NCs. Interestingly, the top NC for this plane, appears to be affected to a large extend of the boundary of the two NCs, since the varying contrast seems to almost originate from the interface between the top NC and the middle one.

The NC-structure in **(g-i)** is two merged NCs consisting of the bottom and the middle one. The planes $< 1\bar{1}0$ and $10\bar{1}$ appear to indicate a boundary at the interface between the NCs, shown by the curved intensities formed in the bottom NC. The latter plane, being the plane which is directed parallel to the longitudinal axis of the Nc-structure, is exactly the direction of the corners used to merge the two NCs.

In **(a-c)**, there is comparably less intensity variations than that of the NC-structure in the second column. In the middle NC there is a repeating pattern of dark and white lines. This signature is a typical sign of superimposed crystal planes which are slightly different, called a Moiré pattern. Such patterns are typically present due to dislocation manifestation, meaning it can be a sign of strain-relevance. It could then be an explanation of why this structure exhibits so little contrast variations compared to the others, due to lattice relaxation. A close-up of the Moiré patterns is shown in **Fig. 24**. Here first- column **(a-c)** is identical to the first column in **Fig. 23**, but with dashed boxes encapsulating the part shown in their respective panels *(i-iii)*.

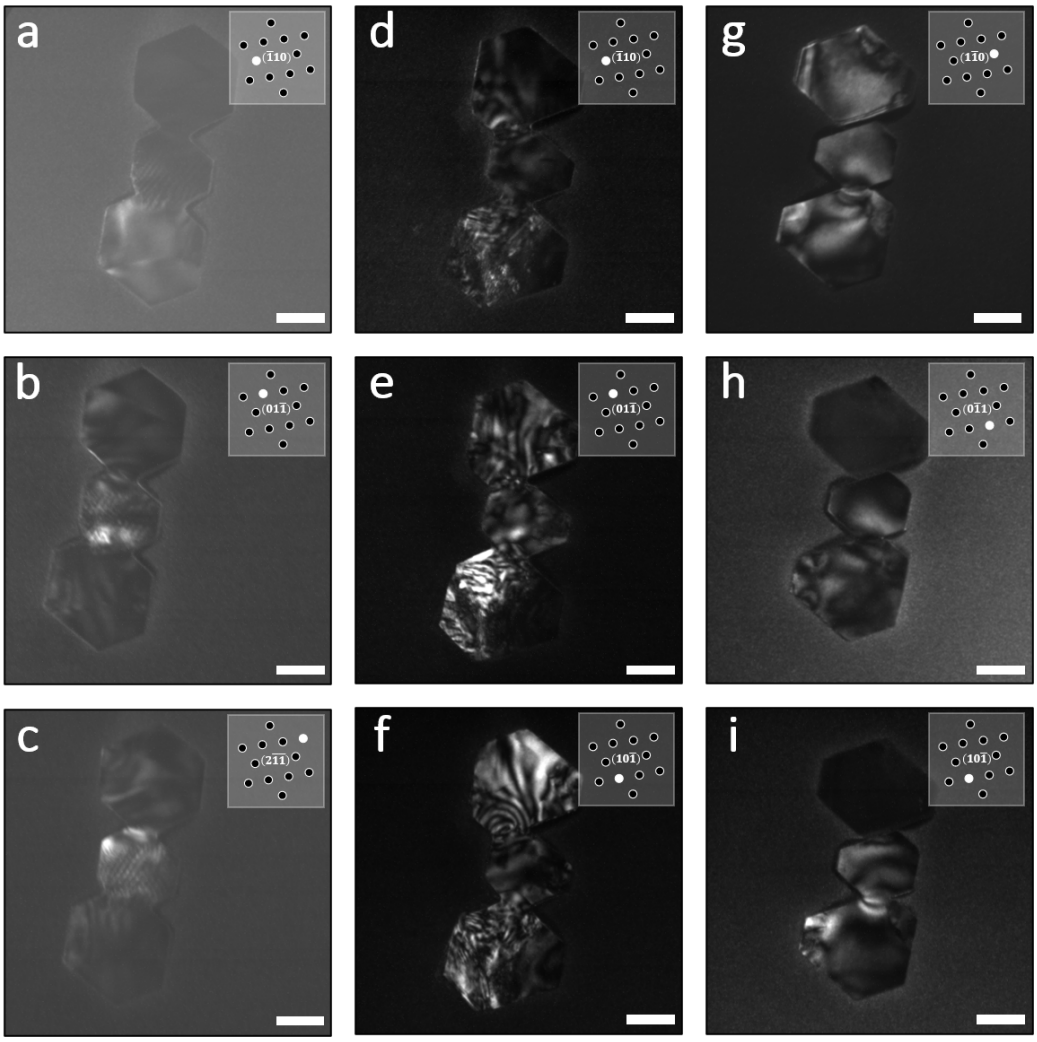

Fig. 23: Bending contours in dark-field. In (a-c), (d-f) and (g-i) the same NC structure is presented as TEM DF micrographs. Every micrograph is aligned to the middle NC high-symmetry zone axis [0001], and the insets indicate which crystal plane the DF is made of

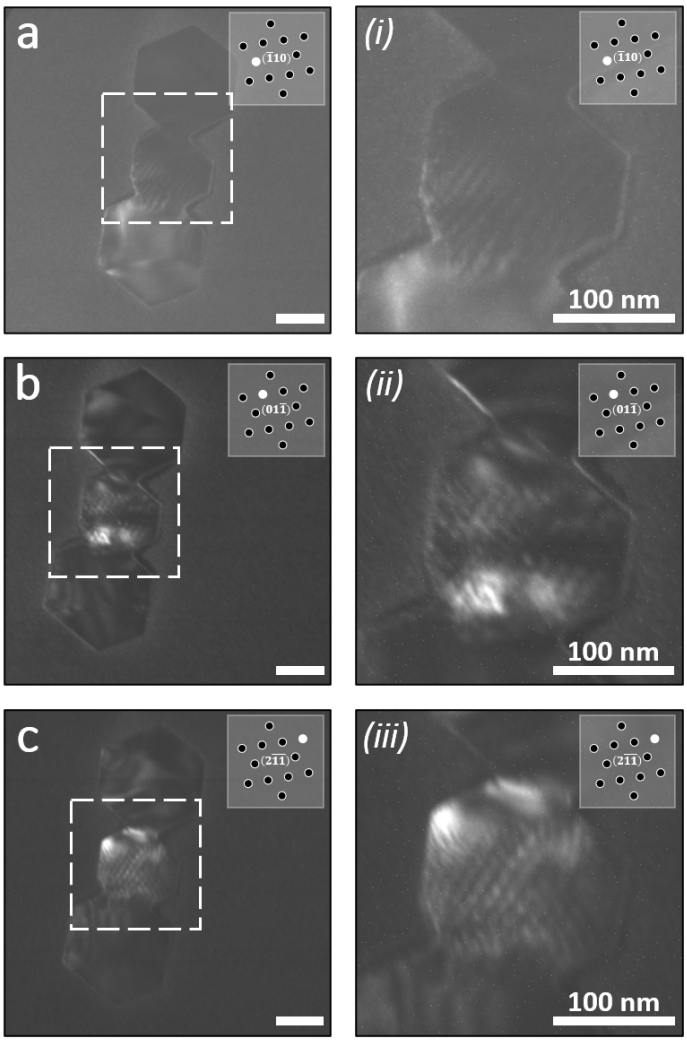

Fig. 24: Moiré pattern. In (a-c) are shown DF micrographs with the middle NC aligned to its high symmetry zone axis. The insets show the crysl plane of the diffracted electrons in DF. The panels *(i-iii)* are close-ups of the white dashed square as indicated in (a-c), respectively. Scale bars are 100 nm.

Since moiré patterns are typical large-scale manifestation of small-scale variations, then in terms of a crystal it translates into two sets of superimposed crystal planes of varying interplanar pitches, different lattice constants or relative rotation[32]. An enlarged view of the middle NC shows that the fringes are extremely dynamic in the sense that across a boundary between two NCs the fringes are distorted indicating alternation of lattice spacings. In other words, it indicates that the lattice experiences an increasing bending of the lattice across two NCs while in the center of a NC less distortion occurs. The fringes manifest in the SAED pattern as extra spots in the crystallographic direction of the fringes themselves. The varying intensities of the SAED spots could be due to improper sample tilt resulting in varying scattering intensities, or it could be because of varying abundance of such diffracting planes.

7.4 Strain indication of merged InAs nanocrystals' crystal lattices

Inspecting the SAED patterns of each NC (the top, middle and bottom) of the structure in **Fig. 22(b)**, as an example, does show some small differences with respect to the reference NC in section 7.2. Although, the standard method for extracting the interplanar spacings of the crystals is by measuring just that in direct space of a HRTEM, or something similar, a reciprocal space analysis could give insight to this behaviour as there is an indirect relationship between the interplanar spacing d_{hkl} and the magnitude of the reciprocal vector $\rightharpoonup g$, as simple as $|\rightharpoonup g| = \frac{1}{d_{hkl}}$.

For a SAED pattern analysis to work in this way it is vital to realise that a standard low-resolution TEM is not able to distinguish the phase differences of each plane, meaning the SAED patterns as shown are averages of the crystal structure. Hence, if any indications of differences in interplanar spacings is supposed to be observable then the entire probed structure has to exhibit such properties. Under this assumption, we compare the magnitudes of the reciprocal space vectors with the reference one just as one usually would do for interplanar spacings $\Delta g = \frac{g^{hkl} - g_0^{hkl}}{g_0^{hkl}}$, where g^{hkl} and g_0^{hkl} is the reciprocal lattice vector to the plane (hkl), and the reference reciprocal lattice vector to the plane (hkl), respectively.

An in-depth analysis of one of the NC-structures is shown in **Fig. 25**. The structure displays hexagonal NCs with diameters of approximately 232 nm, 178 nm and 225 nm, measured of each NC starting on the the top NC. The inspection of each NC consists of aligning the electron beam to the high symmetry zone axis ZB[111]/WZ[0001] as shown in **(a,c,e)** each with their corresponding SAED pattern shown in **(b,d,f)**. Owing to identical in-plane structure of both ZB and WB along the growth direction, polytypism is a common phenomenon in InAs NWs[27][10]. Since the crystal structure of both cubic ZB and hexagonal closed pack (HCP) WZ is identical in the growth direction, it is unclear from the SAED patterns, which one it is[11]. In order to confirm which crystal type the NCs exhibit, one is required to change orientation from an axial point of view to one that is aligned to one of the facets or corners of the NC. The top panel has the top NC aligned to its high symmetry zone axis; the middle panel has the middle NC aligned to its high symmetry axis; and the bottom panel has the bottom NC aligned to its high symmetry axis.

Under the assumption that the magnitude of the reciprocal lattice vectors are anything to go by, both the top **(a,b)** and the middle **(c,d)** NC exhibit comparable reciprocal lattice vector magnitudes within their own NC of the $< 1\bar{1}0 >$ directions as $g_{avg}^{Top} = 0.622 \pm 0.0014$, and $g_{avg}^{Mid} = 0.609 \pm 0.0012$, respectively.

These uncertainties, or spreads of values as they really are, are both below the combined uncertainty inherent to the process of obtaining the data of $\sigma_{ref} = 0.0021$, as extracted in section 7.2. Considering that everything, right from the process of obtaining the TEM micrographs to the

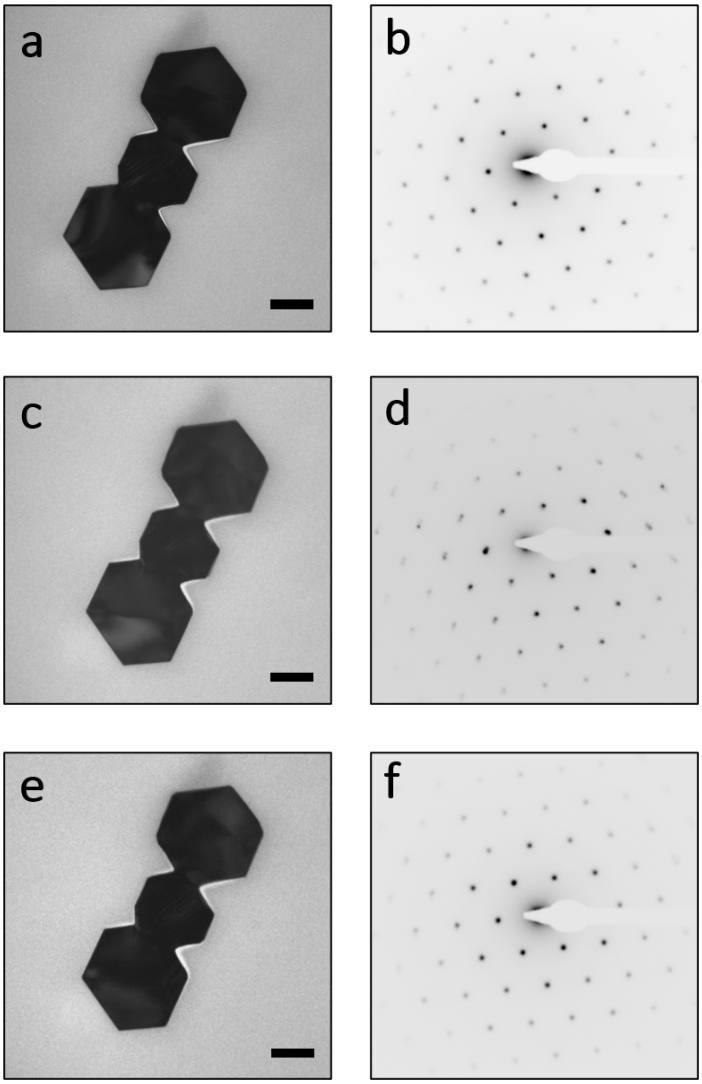

Fig. 25: Nanocrystal structure SAED inspection. In (a-c) the NC that is aligned to their high symmetry zone axis is the one at the top, middle, and then the bottom, respectively. (b-f) shows the corresponding SAED patterns of (a-e), respectively. Scale bars are 100 nm.

methodology of extracting data from them, has been identical, it sounds reasonable that σ_{ref} is transferable between each SAED analysis, and could potentially act as a guide, or indicator, of when the magnitudes of the reciprocal vectors of similar planes e.g. $< 1\bar{1}0 >$ are reasonably close to be classified as being identical.

If applicable in this way, then the top and middle NC each exhibit comparable reciprocal lattice vectors within their own SAED pattern. Additionally, both of these NCs appear the indicate a compressed or expanded crystal lattice in comparison to the reference structure, as discussed in section 7.2, with relative reciprocal lattice vectors of $\Delta g^{Top} = 1.1 \pm 0.2\%$, and $\Delta g^{Mid} = -1.0 \pm 0.2\%$. A positive value corresponds to an elongated reciprocal lattice, which means that the lattice planes in direct space is compressed, and vice versa.

The bottom NC acts differently. The SAED pattern of the NC appears to have differently varying crystallographic directions of the $< 1\bar{1}0$ type, as indicated by the relatively large spread of the averaged reciprocal lattice vector magnitude $g^{Bot}_{avg} = 0.609 \pm 0.0032$, which is on average a $\frac{3}{2}$ larger spread than the reference σ_{ref}. A large spread can be indication of relatively large variations of the reciprocal lattice vectors, where the planes parallel to the $(10\bar{1})$ plane appear to be the most affected $\Delta g^{Bot}_{(10\bar{1})} = -1.5\%$, and for the planes parallel to $(01\bar{1})$ with $\Delta g^{Bot}_{(01\bar{1})} = -0.8\%$, and parallel to the $(\bar{1}10)$ plane $\Delta g^{Bot}_{(\bar{1}10)} = -0.6\%$. The one with the larges deviation with respect to the reference NC, is in the direction along the long axis of the entire NC-structure potentially indicating the merging of the bottom and middle NCs to affect the crystal lattice by straining it in a compressing manner.

The qualitative assessment of the structure has already been discussed in the previous section 7.4 by the use of BF and DF micrographs addressing the intensity variations with relation to induced strain. In respect to the values listed above, the small intensity variations of each NC could be related to the relatively comparable reciprocal lattice vectors of the top and middle NC, respectively, indicating similar stress-induced strainage in their respective crystallographic orientations. The bottom NC appears to exhibit larger strain variation in the crystal as indicated by the -1.5% deviation from the reference NC in the $(10\bar{1})$ plane, being considerably larger than the others. The contrast variation as indicated by the BF (**Fig. 25**) and the DF (**Fig. 23**(a-c)), could explain such large deviation of the reciprocal lattice vectors. In addition, for the middle NC, moiré patterns are observed (**Fig. 24**) indicating a possible relaxation by dislocation, which also could potentially account for the similar reciprocal lattice vectors of the $< 10\bar{1} >$ type.

Applying the same SAED analysis on a different NC-structure, as shown in **Fig. 26**, every single NC exhibit a relatively large spread of reciprocal lattice vector values. Although the top NC is disconnected from the rest, the average reciprocal lattice vector magnitude of the $< 10\bar{1} >$ type is $g^{Top}_{avg} = 0.608 \pm 0.0031$, which is about $\frac{3}{2}$ larger than the reference uncertainty σ_{ref}. The largest deviation with respect to the reference NC in the crystal is found in the direction of the $(01\bar{1})$ planes, deviating with $\Delta g^{Top}_{(01\bar{1})} = -1.6\%$, and for the direction of the $(10\bar{1})$ plane there is a $\Delta g^{Top}_{(10\bar{1})} = -1.2\%$ with respect to the reference NC, and finally of the $(\bar{1}10)$ plane, the deviation is quite small $\Delta g^{Top}_{(\bar{1}10)} = -0.6\%$. Hence, all show indications of enlarged crystal lattice in direct space.

For the two merged NCs (i.e. middle and bottom NCs), they exhibit quite similar tendencies. Both exhibit large spread of reciprocal lattice vectors of the $< 10\bar{1} >$ type. The average values are $g^{Mid}_{avg} = 0.607 \pm 0.0044$, and $g^{bot}_{avg} = 0.607 \pm 0.0039$, both close to having spreads double of the uncertainty related to the process σ_{ref}. This could be indicative of relatively large strainage effects in the respective NCs.

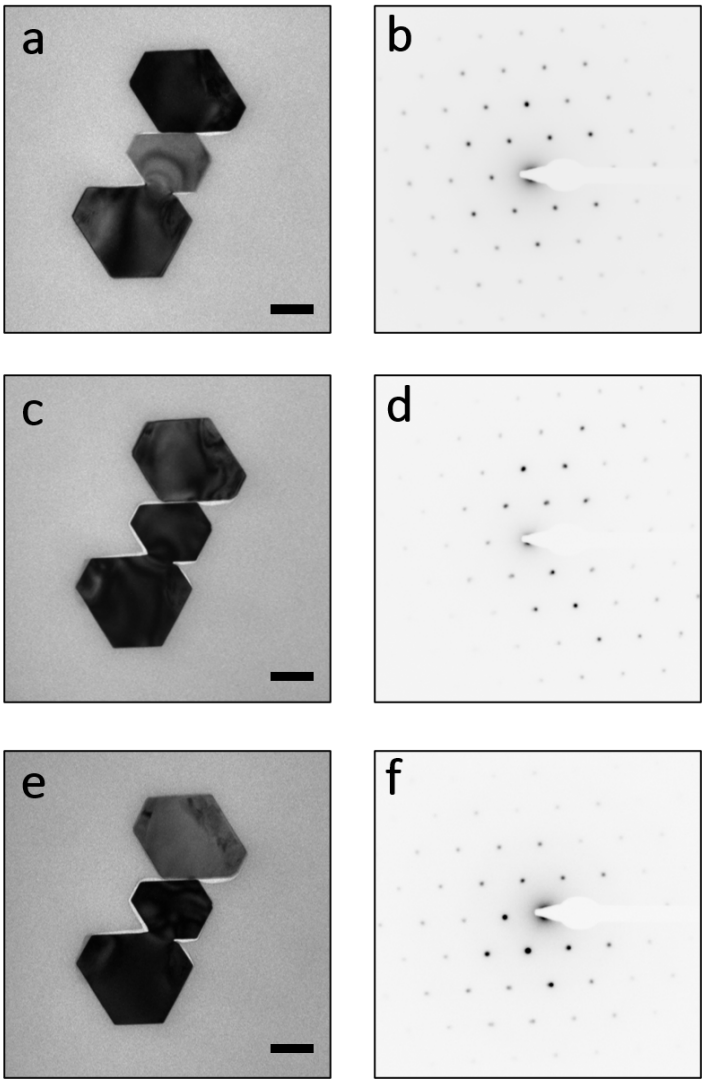

Fig. 26: Nanocrystal structure SAED inspection. In (a-c) the NC that is aligned to their high symmetry zone axis is the one at the top, middle, and then the bottom, respectively. (b-f) shows the corresponding SAED patterns of (a-e), respectively. Scale bars are 100 nm.

Remarkably, their deviations from the reference values of the single NC in section 7.2 follow the same ordering in respect to the crystallographic planes. The direction, which exhibits the larges deviation is parallel to the plane $(10\bar{1})$ of $\Delta g^{Mid}_{(10\bar{1})} = -2.1\%$, and $\Delta g^{Bot}_{(10\bar{1})} = -2.0\%$, for the middle and bottom NC, respectively. The second-most affected direction is in the direction of the $(01\bar{1})$ planes of $\Delta g^{Mid}_{(01\bar{1})} = -1.0\%$ and $\Delta g^{Bot}_{(01\bar{1})} = -1.0\%$, respectively. And for the $(\bar{1}10)$ planes of the two NCs, the deviations from the reference NC are $\Delta g^{Mid}_{(\bar{1}10)} = -0.7\%$, and $\Delta g^{Bot}_{(\bar{1}10)} = -0.8\%$.

All of this values are indicative of an enlarged direct lattice spacing of either NC. The remarkable thing about the two merged NCs, is their similar values in every direction, and the fact that the largest deviating directions of the $(10\bar{1})$ planes are in the direction of the corners used to merge the two. See **Fig. 26(c,e)**. In the DF micrographs of this NC-structure, if the $(10\bar{1})$ plane is isolated to observe the diffracted electrons of those planes (**Fig. 23(i)**) the most intense illumination is in fact observed at the merged junction. Hence, it indicates a large crystal lattice bending potentially as a consequence of the the merging of the two NCs.

Although scarce on data, some tendencies are observed for this kind of SAED analysis. In general for the cases of the NC-structures consisting of NCs conjoined by the corners, when they exhibit reciprocal lattice vector of the $< 10\bar{1} >$ type with relatively large spreads of distances for the individual NC, the largest deviation in respect to the reference NC, is in the direction of $(10\bar{1})$ planes, which coincidentally is along the path of the longitudinal axis of the entire structure. This does not have to be odd, as previous studies on core-shell structures indicate that the larges in-plane strain is found centered around the corners of a hexagonal NW core, as well as relatively large values at the facet interface[1],[29]. However, when the merging of NCs excedes beyond the corners, but incorporates the facets as well (see **Fig. 22(e,f)**), the reciprocal lattice vector deviations from the reference NC increases. In this case with averages of $\Delta g^{Bot} = -3.3 \pm 0.6\%$, and $\Delta g^{Bot} = -3.3 \pm 0.7\%$ (see **Fig. 22 (e,f)**, respectively), which could play in hand with a reduced elastic modulus for larger structures[45], resulting in more readily distorted structures as a result of experienced shear stress. Consult the Appendix for the raw data of all of the SAED analyses.

7.5 InAs/AlSb/InAs Core Double Shell Architecture

In this section the focus will still be on cross-sectioned NWs, but only for a different system. A break or damage to the specimen, or material, during slicing it using the Microtome is unacceptable. The mechanical properties of the material is therefor extremely important. Studies on various materials have been reported, and for the cases of In, As, Al and Sb, they have either been classified as being intact or predicted to remain intact after sectioning[12].

Combining different semiconductors and metal alloys to engineer and manipulate the band line-ups offers a broad variety of complex heterostructures. Since InAs and AlSb have different band-gap energies of 0.36 eV and 1.61 eV, respectively, and AlSb haveing its conduction band edge 1.35 eV above that of InAs, they will theoretically form an extraordinarily deep quantum well with high tunneling barriers[28]. In fact, compared to an Sb-alloy counterpart of GaSb, which would form a less deep quantum well, the InAs/AlSb quantum well can posses similar or even higher electron mobilities. This is likely due to surface donors residing in the capping layer - in our case of InAs - transferring into the quantum well thereby increasing the pinned fermi level inside of InAs[49],[35]. Due to a staggered type-II band alignment of this heterostructure, the electrons and holes are effectively separated, with the holes trapped in the AlSb valence band and electrons residing in the conduction band of InAs[30]. The InAs capping layer is important to passivate the InAs/AlSb

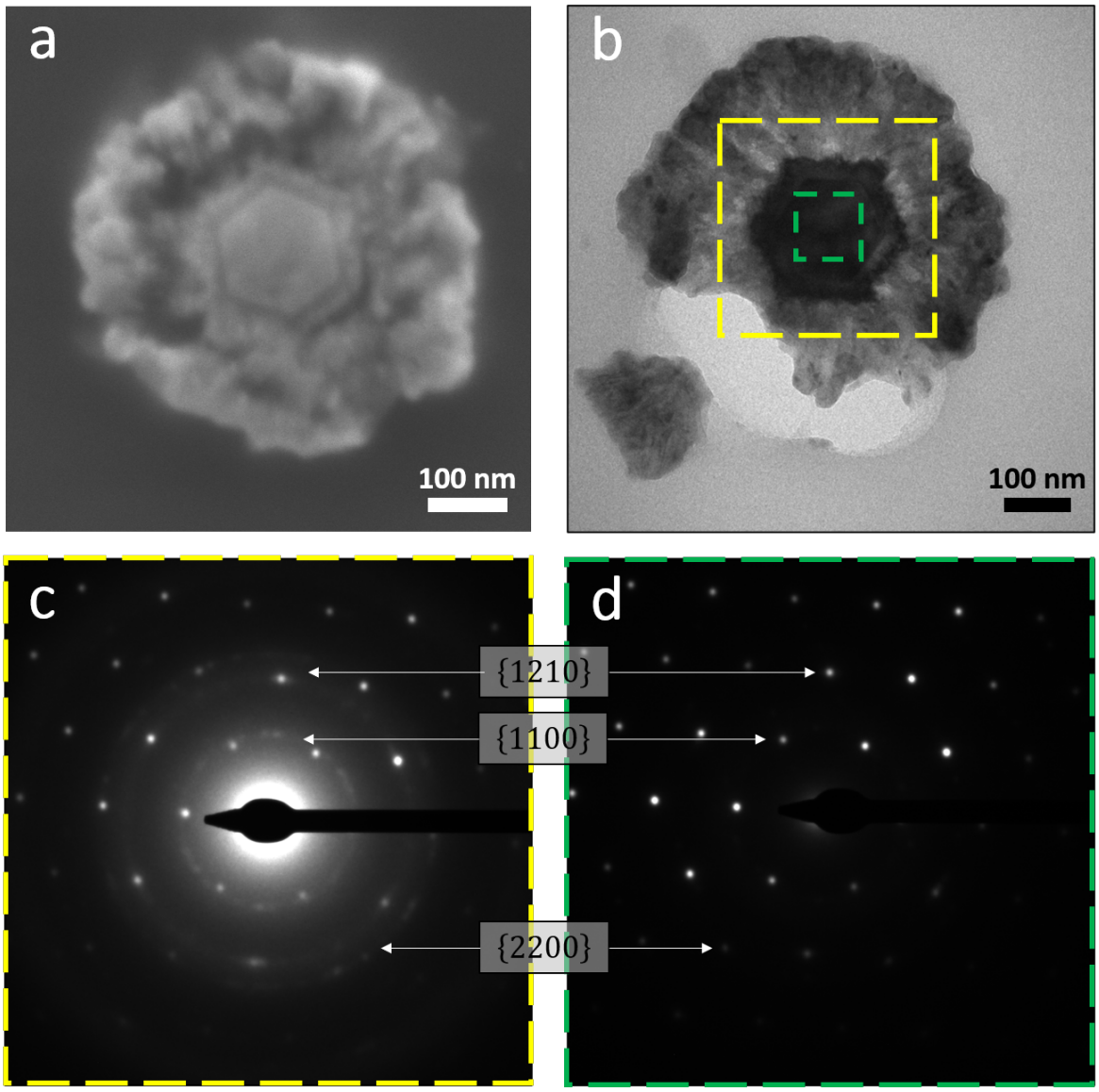

Fig. 27: InAs/AlSb/InAs. In (a) is shown a SEM image, where in (b) is shown a TEM micrograph of an InAs/AlSb/InAs heterostructure. In (b) SAED patterns are obtained from the color-coded dashed squares. (c) shows signatures of polycrystalline material, whereas (d) only shows the SAED pattern of the InAs core.

quantum well, as the Al of AlSb easily oxidizes.

In **Fig. 27** cross-sectional views of two different InAs/AlSb/InAs grown NWs; one observed using an SEM, and the other a TEM **(a,b)**, with corresponding SAED patterns of the InAs core and of a larger area including both the shell and the core outlined by color-coded dashed boxes **(c,d)**. The SEM micrograph **(a)** probes the surface and displays contrast mostly depending on a combination of topography and density. Assuming a uniform, and relatively horizontal cutting motion of the Microtome, it is assumed that the major contrast influence is due to the density of the specimen. The core exhibits slightly lighter intensity than attached shell, which is likely due to Sb being heavier than In or As. The outer-most flower-like shell displays high contrast, likely to originate from Al reacting with oxygen. The grainy structure of the outer-most shell is similar in style with oxygen rich Al regions under TEM and SEM investigation[6],[23].

The SAED patterns **(c,d)** corresponding to different inclusions of the CS heterostructure in **(b)**, show an InAs core aligned to its high-symmetry zone-axis ZB[111]/WZ[0001]. Due to polytypism and identical crystal structure in the growth direction, it is unknown whether the InAs is in the WZ or in the ZB phase. The AlSb also exists in WZ or ZB phases[24]. If the InAs core and the AlSb were to exhibit different crystal phases, then there would be a 30° rotation between identical patterns. However, this is difficult to determine, as the rings of certain crystallographic planes indicate polycrystalline material **(c)**. The polycrystallinity is likely to be attributed to the AlSb shell, as these rings are not present in the SAED pattern of the InAs core. It has been reported that tensile stress can induce dislocations, which consequently can render a single crystal into a polycrystalline material[33]. Although, it is speculative, it could be that the oxidative process of Al in AlSb deforms the crystal into an amorphous structure, which is accompanied by a metal-oxide interface of AlSb-Al_2O_2 with a different interface potential[20] than metal-metal. Due to such a change of environment, it could cause there to be varying stress-fields in the crystal of tensile and compressive kinds, potentially resulting in a transformation of a single crystal to a polycrystal.

Even though bulk InAs and AlSb exhibit a small crystal lattice mismatch of only 1.3 %, at the interface of the two semiconductors, large strain is present due to no shared elements of each compound. The optical and electronic properties of InAs/AlSb heterostructures are drammatically affected by the type of interface. The different bond types of Al-As and In-Sb have vastly different bulk lattice mismatches of -6.6 % and +6.9 %, respectively. Thus, the type and extend of interface bonding can be responsible for large local distortions[50], [43], [36]. Since devices are highly sensitive to the structural and chemical properties of their interfaces, a seemingly film consisting of Aluminium oxide on the heterostructure interface[20], as shown in **Fig. 27**, can alter the properties of the intended deep quantum well.

In the following sections, the electron transport is investigated of the serial conjoined InAs NCs, and of the heterostructure discussed here.

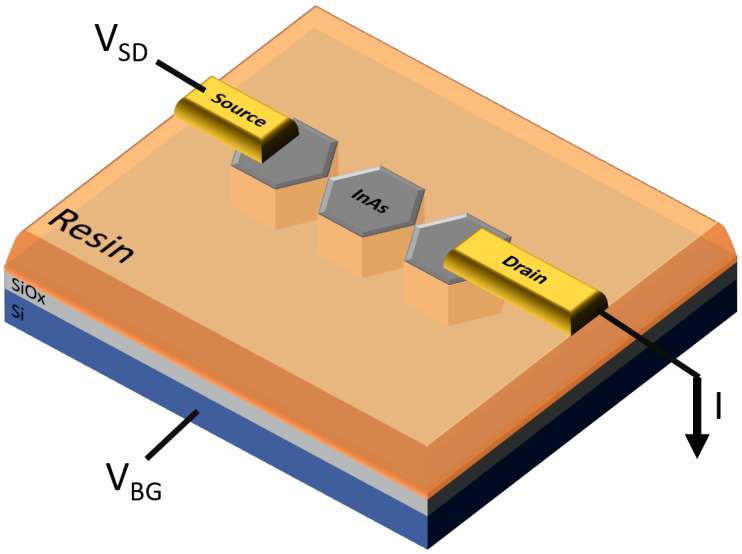

Fig. 28: A typical depiction of a field-effect transistor device investigated. The graphic shows three InAs nanocrystals (dark grey) in series surrounded by resin, however in most of the cases in this work the channel consists of one to three nanocrystals, which either have a small gap between them or are merged together to some extend. A simple illustration of the electrostatic voltage sources and where they are applied. A bias current is controlled by the source-drain voltage applied to the Ti/Au (5/200 nm) electrodes (golden), and a voltage is applied to the Si back-gate which capacitively couples to the InAs nanocrystals by setting up an electric field through the SiOx layer.

8 Electron Transport in Nanocrystals

A presentation of not-so-succesful devices, but there might be something to work with in the future.

As previously described (in section: Fabrication) the fabrication of nanoskived nanowires proves difficult with a multitude of challenges, and not all kinks of the process has as of yet been illuminated. Consequently, working devices is presently a rare sight. Nevertheless, every once in a while some do in fact show show conductive properties, and these devices are the ones in focus in this section.

All of the NCs investigated are of similar type; they are all two-terminal devices with Ti/Au (5/200 nm) source and drain contacts along with a global back-gate, as depicted in **Fig. 28**. The sectioned wires themselves vary greatly, however. The length, diameter, inter-wire separation are all parameters which vary - all of which are discussed in section (section: Device fabrication and its challenges).

Due to the challenging part of fabricating devices not all sets of devices came out as hoped, and not all devices came out as hoped in the very same processing run. An overview of such processing run is illustrated in Table 2, where a high yield is something to be missed. Here, six devices exhibited metallic contact with linear current response to applied bias voltage. However, after cool down to 2.6 K one of those devices lost its linear response and remained a constant current even at varied bias voltages. The other five devices remained their linear behaviour. The five out of 21 devices in total for that particular processing run means a success rate of 24 percent - With

Device ID	Nanocrystals	Source-drain separation [nm]	Resistance [kΩ]	Average $2G_0$
11	1	120	2.44	0.05
13	2	256	5850	0.001
16	n/a	68	1.45	8.6
17	n/a	n/a	2.47	4.8
18	2	94	846.4	0.01
19	1	102	1.49	8.3

Table 2: Room Temperature Data. Plenty of challenges surround the fabrication of devices made of nanoskived nanowires. To illustrate the rate at which successful devices are fabricated for a single processing run, here are shown six different devices of a complete set of 21. For each device room temperature (RT) measurements were performed, and for those showing metallic character, a linear curve was fitted to extract the resistance of each device. The number of nanocrystals each device consist of indicate the expected barriers formed as well as the separation between each electrode are listed. The 'n/a' indicates when a specification is unable to be obtained for various reasons.

so few functioning devices it is difficult to tell what does the trick. Having already addressed the issues in previous chapter (SECTION: device fab and challenges), it becomes clear what to avoid to successfully fabricate devices. The remaining of this chapter is focused on a closer look on some of these functioning devices.

8.1 Room Temperature Response

As mentioned in the introduction of this chapter only a hand full devices of a single processing run showed ohmic behaviour. The metallic characteristics can be seen in **Fig. 29**. In **(a)** is shown six devices with linear responses to bias voltage, although some are more linear than others. The less-perfect linear responses are framed with a dashed box, and shown in **(b)**. Linear functions have been fitted to the data to extract the resistances, which are shown in Table 2. It is worth noting that device 13 is close to having a flat curve, which more-or-less tells that it is not very responsive to the bias. At cryogenic temperature of 2.6 K, it no longer exhibits a similar linear response, but is completely unresponsive (see SUPPLEMENTARY INFO). In **Fig. 30** some of the devices is displayed. The other devices are difficult to view as resist covers them completely or missing NCs after measureing (see SUPPLEMENTARY INFO). In **Fig. 30** they all exhibit different structural characteristics. Device 11 **(a)** consists of a source-drain channel length of 120 nm, and exhibits a resistance of 2.44 kOhms at RT. Unfortunately, the sectioning directions was close-to parallel with the long axis of the entire NC structure, which is probably the reason for the crevasse at the center of the device. Device 18 **(b)** exhibit relatively large resistance of 846 kOhms. The channel appears to have a small 2 nm gap in between the NCs. Several other non-functioning devices also appear to have gaps between the electrodes, but non as small as 2 nm (see SECTION: DEVICE FAB AND CHALLENGES). Device 19 **(c)** is a different case than the two others, as this one at first glance appears to be a single NC, which exhibits one of the smallest device resistances at RT of 1.49 kOhms.

....

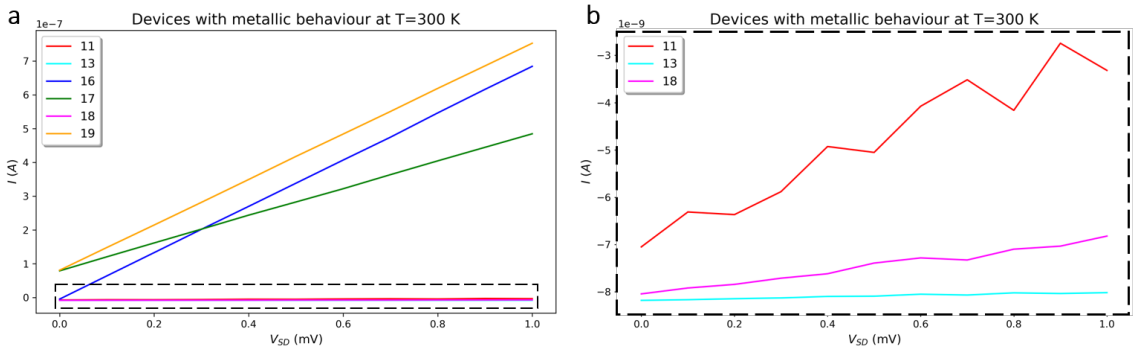

Fig. 29: Linear I/V characteristics. In **(a)** is shown all of the devices with metallic characteristics for a specific processing run, with the dashed box focused on three of the devices to be enlarged in **(b)**. The legends are device IDs. Devices 16, 17 and 19 all have what appears perfect linear responses, whereas devices 11, 13 and 18 have not. Note the y-axes: **(a)** is in 100 nA, and **(b)** is in nA.

8.2 Quanutm Phenomena in InAs Nanocrystal Devices

Reducing the temperature to that of the cryogenic kind reduces thermal excitations and lowers the phonon vibrations in the crystal lattice, and will allow access to the finer electron transport characteristics of the InAs NC. In this section the focus will be on Device 11 as it exhibits pronounced quantum dots signatures and resemblance of Fabry-Perot oscillations. In addition, the other devices discussed in the previous section will also be highlighted as they did exhibit some interesting quantum transport phenomena, although faint due to current leakage to the back-gate greatly limiting the measurements.

8.2.1 Nanocrystals in Series as a Device

The most promising device fabricated on a series of InAs NCs is the one shown in **Fig. 31 (b)**. The figure illustrates the sectioning process with **(d)** displaying graphically what slice number of the nanowire was used. The very first adequately shaped slice, as described in Section **??**, is defined to be at zero and can be seen in **(a)**. Four hundred nm into the sectioning, and the corresponding wire-structure as seen in **(a)** is located and used for device fabrication, as shown in **(b)**. The red dashed outline indicates the part of the wire used for device fabrication. The keen eye will notice, that the wire used for the device is mirror-imaged, as can be seen in the inset of **(b)**. It is likely that the lamella itself, containing the wires, flipped on its head during transferring of it the the device substrate. A single section further into the sectioning, and the very same wire is seen in **(c)**. As is clear from the showings of the cutting process of this particular wire (see the red arrows), the continuous exertion of pressure or stress applied to the wires resulted in a continuously degrading of the wire structural integrity. It should be noted that the cutting direction of this particular sectioning process was along the long axis of the structure, i.e. more-or-less parallel to the wires. The white arrow in both **(a,b)** serves as a guide to the eye tracking the striation across the wire. At the section of 500 nm (see **(c)**) it is less clear where this striation is, as more of them has appeared; likely a consequence of the cutting process resulting in fractured wires. It should be noted that a

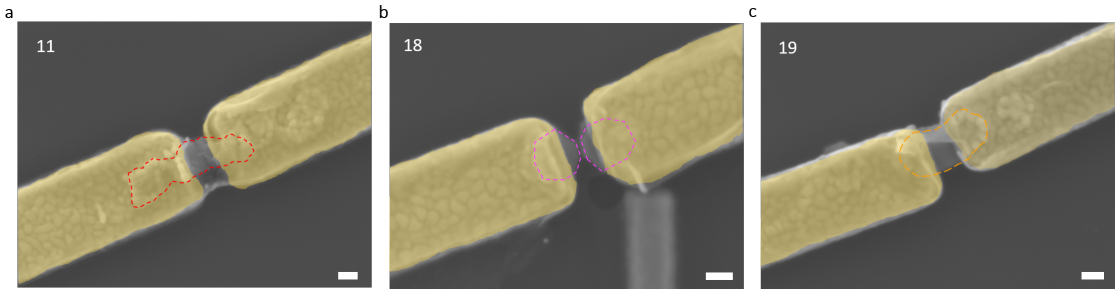

Fig. 30: Metallic devices. False-colored electrodes. Some different NCs turned into devices with metallic characteristics as can be seen in **Fig. 29**. In **(a)** is device 11, **(b)** is device 18, and **(c)** is device 19. Devices 11 and 18 appear to have relatively high metallic resistances, whereas device 19 exhibit a much lower one. All three of the devices exhibit some structural differences; 11 looks to have a crevasse in its conducting channel; 18 appears to have a gap in-between the two NCs of about 2 nm; and 19 consists of a single NC, which is likely a merging of two NCs. The dashed outlines display the size of the NCs, and the colors refer to their I/V-characteristics in **Fig. 29**. Scale bars: 100 nm.

third section was transferred to a TEM grid, but unfortunate placement of the lamella meant that the exact wire corresponding to the ones shown in **Fig. 31** was lost. See Appendix section **??** for an expanded version of figure **Fig. 31** including SEM and TEM of a different wire of the same cutting process tracked across different sections. Clearly visible barrier at the junction of two NCs emerge in the TEM micrograph which is not visible using the SEM.

8.2.2 Electrostatic Gating

The device under investigation, shown in **Fig. 31**, is a two-terminal device with a global back-gate. Manipulating the electrostatic potential of the device clearly alters the conductance as seen in **Fig. 32**. In **(a)** is shown four sets of zero-bias conductance all with up- and down sweeps. Each set is separated by 0.2 conductance due to hysteresis, as all sweeps displayed on the same horizontal line (i.e. no separation) would result in a jumble of conductance peaks. The darker tones are down sweeps, and in general tend to remain more stable over multiple sweeps in contrast to the up sweeps. Nevertheless, as indicated by the black vertical arrow, subsequent sweeps performed one after the other increases the stability. The instabilities and hence the variations of the potential landscape can also be seen in Appendix section **??**. The two back-gate voltage areas under investigation are the ones marked with dashed boxes: panel (i) and panel (ii). Panel (i) and panel (ii) are enlarged in **(b)** and **(c)**, respectively. The reasoning for the panel outlines placements in **(a)** is because the bias-spectroscopy measurements performed at these gate voltages were performed right after those individual sweeps, and perhaps serve to better describe the data. As is clear from these two panels is the hysteresis of the earlier sweeps, whereas subjecting the device to multiple bias sweeps in a row increases stability. In addition, the high positive voltages applied by the back-gate strongly affects the sizes of the conductance peaks, which could be due to stronger couplings to each energy level in what resembles signatures of a quantum dot due to alternating conductance peak formation and near-zero conductance regions in-between. Typical character of single-electron tunneling.

After performing some stabilizing up and down bias sweeps, two conductance resonances inside

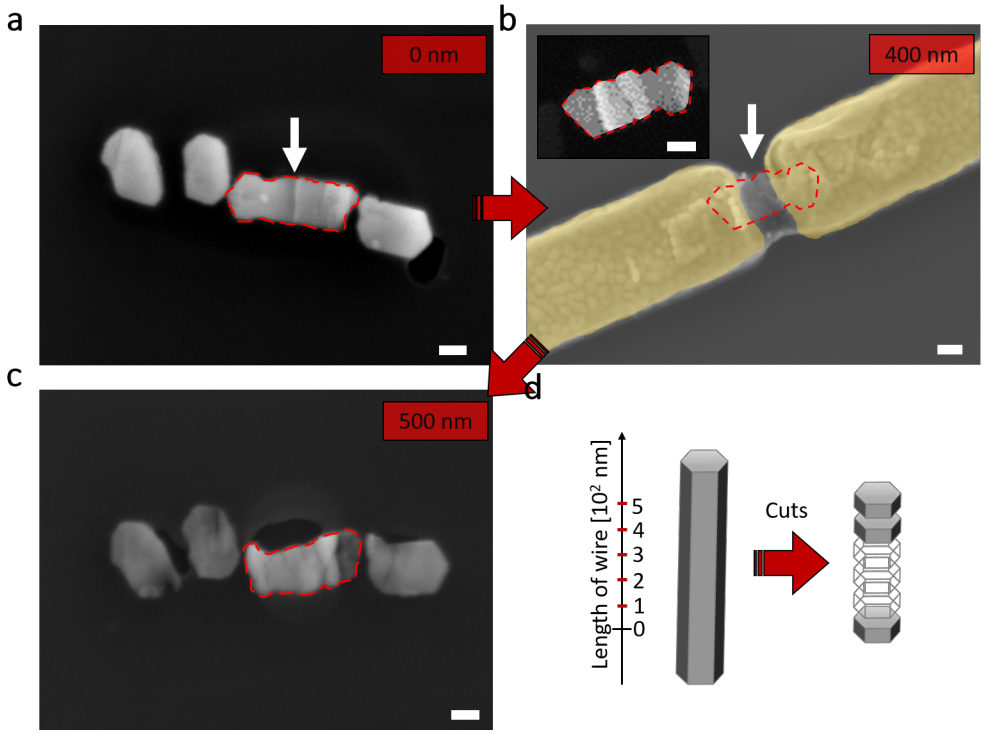

Fig. 31: Cutting Flow Process of the Device. Sections of the same wire are obtained showing morphological variations as the cutting went on. **(a)** SEM image of the wire used for device marked with red, dashed outline cut 400 nm lower/earlier on the wire. This sectioning height is defined as zero. **(b)** device made on section cut 400 nm above the defined zero. Red outline marks the device size, and is the corresponding part marked in **(a)**. The white arrows on these two images show a possible fracture due to the cutting process. The inset of **(b)** is low resolution, fast and automated SEM image of the wire used for the device. Here, the alleged fracture is more prominent. **(c)** the following section, now at 500 nm above structure shown in **(a)**, exhibit an increased amount of fractures. Nanowire in **(b)** is flipped on its head. **(d)** a graphical illustration depicting the cutting flow of the shown SEM images, with the cutting starting from the bottom of thw nanowire. All scale bars are 100 nm.

of the gate-voltage range of 9.5 V to 12 V were examined, as evidenced in **Fig. 33**. These two peaks are also observed in the bias-spectroscopy measurement performed in the region of panel (i), see **Fig. 34 (a)**, hence the electron number indication of $N + 1$ in **Fig. 33 (a)**. These high resolution measurements (relatively compared to the ones performed in **Fig. 32**) are suited for extracting their width; meaning a quantitative parameter on the peak broadening can be obtained. At low temperature, there are two slightly different equations that can be employed to describe the conductance resonance line shape[19][25]. The first being one describing the resonance due to thermal broadening,

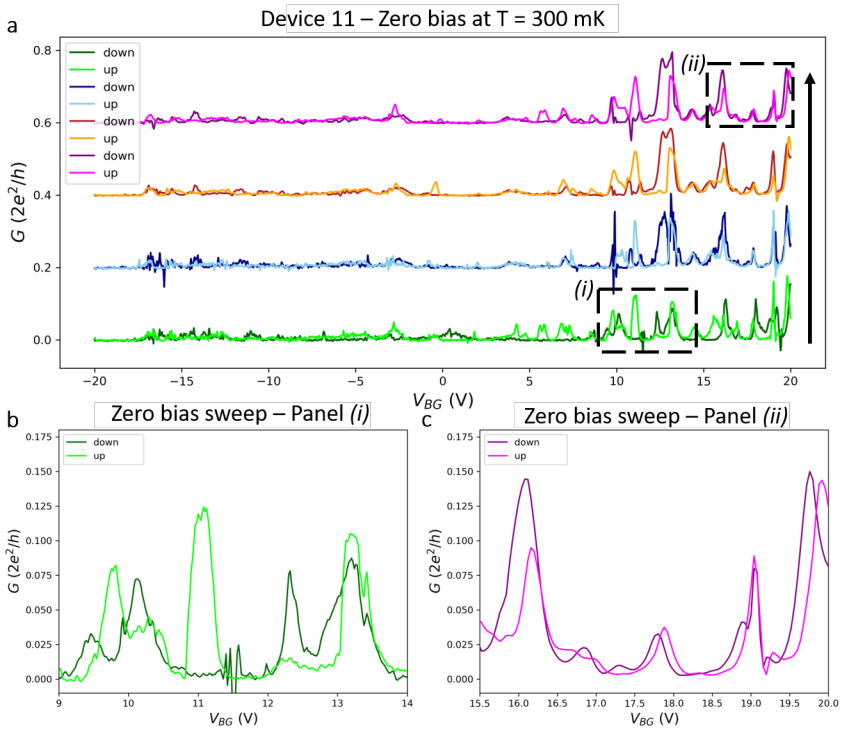

Fig. 32: Linear conductance versus backgate voltage. The device depicted in **Fig. 31** shows hysteric character while varying the back-gate voltage; continuously sweeping up and down. **(a)** shows such behaviour where sweeps are separated into sets of up and down, with the next sets each separated by 0.2 G with respect to the sets coming before them. The vertical arrow indicates the order of sweeping: First down, then up. Repeadetly. The dashed areas marked with (i) and (ii) are both enlarged in **(b)** and **(c)**, respectively. Both of these areas are subject to bias-spectroscopy to be shown later in this section.

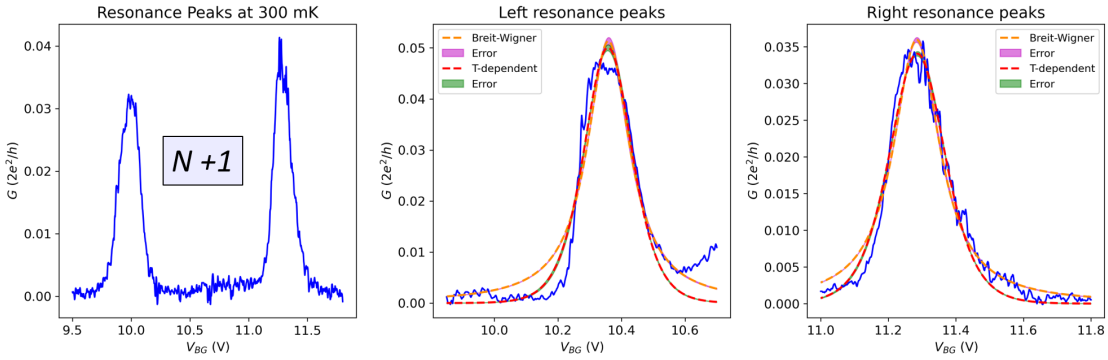

Fig. 33: Conductance Resonances. Two conductance resonances **(a)** are analyzed; one denoted as the left resonance **(b)**; the other denoted as the right resonance **(c)**. Two different, yet similar, fits are deployed as analysis tools. The red dashed fit is a temperature dependent conductance function, whereas the orange dashed fit is a Lorentzian function relying on coupling to broaden a resonance peak.

$$G(V_g) = Cosh^{-2}\left(\alpha\frac{[V_g - V_{g0}]}{2k_BT}\right)G_0 \tag{4}$$

and the second is the Breit-Wigner formula, which is applicable for higher-order tunneling processes, but also works for conductance resonances which are broadened due to coupling of the leads to the single-electron levels of the quantum dot; displaying a Lorentzian resonance line shape,

$$G(V_g) = \frac{2e^2}{h}\frac{(h\Gamma)^2}{(h\Gamma)^2 + \alpha[V_g - V_{g0}]} \tag{5}$$

where, for both equations, $\alpha = \frac{C_g}{C_\varepsilon}$ is the conversion factor with C_g and C_ε being the gate capacitance and the system's total capacitance, respectively. V_g is the gate-voltage, V_{g0} is the gate-voltage position of the resonance; G_0 is the amplitude of the resonance; k_BT is the thermal energy; and $h\Gamma$ is the coupling resulting in broadened resonances.

These two equations both describe the shape of a resonance. For the thermally broadened resonance Eq. 4 the width is simply described by the $FWHM = 3.53k_BT$ which coincidentally is also a measure of the absolute temperature of the electron. For the Breit-Wigner formula Eq. 5 the parameter $h\Gamma$ describes the width of the resonance, which relates to the coupling.

Applying both equations to extract fit parameters result in the fits as shown in **Fig. 33 (b)** and **(c)** where the Eq. 4 is the red dashed line fit, and the Eq. 5 is the orange dashed line fit. Both fits are nearly identical, but considering that the system is cooled down to 300 mK; a thermal energy corresponding to $k_BT = 0.026meV$ it would be unlikely that the majority of the resonance broadenings are consequences of thermal broadening. In addition, the FWHM of the two resonances, acquired from the temperature-dependent fits of Eq. 4, are $\Gamma_{FWHM_L} = 178.1meV$ and $\Gamma_{FWHM_R} = 195.5meV$, respectively. Both of these energies are much larger than the thermal energy $\Gamma >> k_BT$, which illustrates the broadening is not due to temperature, but coupling of the leads to the quantuzed energy levels. The broadening fit-parameters acquired from the Lorentzian

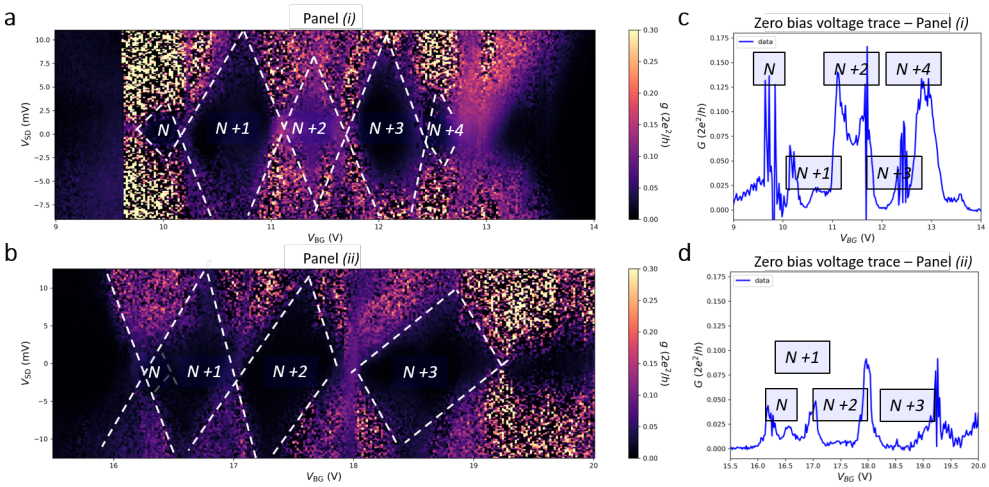

Fig. 34: Caption

line shape Eq. 5 are $h\Gamma_L = 12.2meV$ and $h\Gamma_R = 470.2meV$, respectively. Although smaller than the widths acquired from the thermally dependent fit, they both still are much larger than the thermal energy.

These relatively large energy scales indicates that one can probably expect the excited states of each quantized ground state to be smeared out and therefor non-resolvable in a bias-spectroscopy measurement, as we will see in the following section.

8.2.3 Quantum Dot Signatures in InAs Nanocrystal

As **Fig. 32 (b)** and **(c)** show, both have hysteric behaviour to some extend; one more than the other. This means when doing bias-spectroscopy measurements of these two areas, it can be difficult to estimate the number of coulomb blockade diamonds. This goes mostly for the sweeps in panel (i). Panel (ii) indicates potentially four diamonds. However, as the hysteresis interferes with such qualitative estimations, the bias-spectroscopy performed in each region is accompanied with their zero-bias traces (i.e. not actual measurements but data points from the bias-spectroscopy measurements). See **Fig. 34**.

The traces in **(c)** and **(d)** show resonance-like behaviour, which is likely the indication of quantization of electrons residing on the quantum dot. The numbering is indicated with N since it wasn't possible to deplete the quantum dot, meaning the actual number is unknown. The traces is thus used in order to estimate the number of diamonds in the 2D-sweeps seen in **Fig. 34 (a)** and **(b)**. The diamond sizes along is difficult to predict, as noise limits the visibility. As already discussed, the device itself does not look intact, and is likely very disordered in that regard. It could be that such fractures form multiple unintentional quantum dots, which all would experience some degree of capacitive coupling both to the back-gate, but also the environment producing asymmetrical electrical fields. It also appears that the lead coupling changes vs. gate-voltage, as can be seen by the change of slopes starting as symmetrical diamonds at the gate range of 9 to 14 V, and changing to asymmetrical slopes with stronger coupling to the drain in larger gate range of

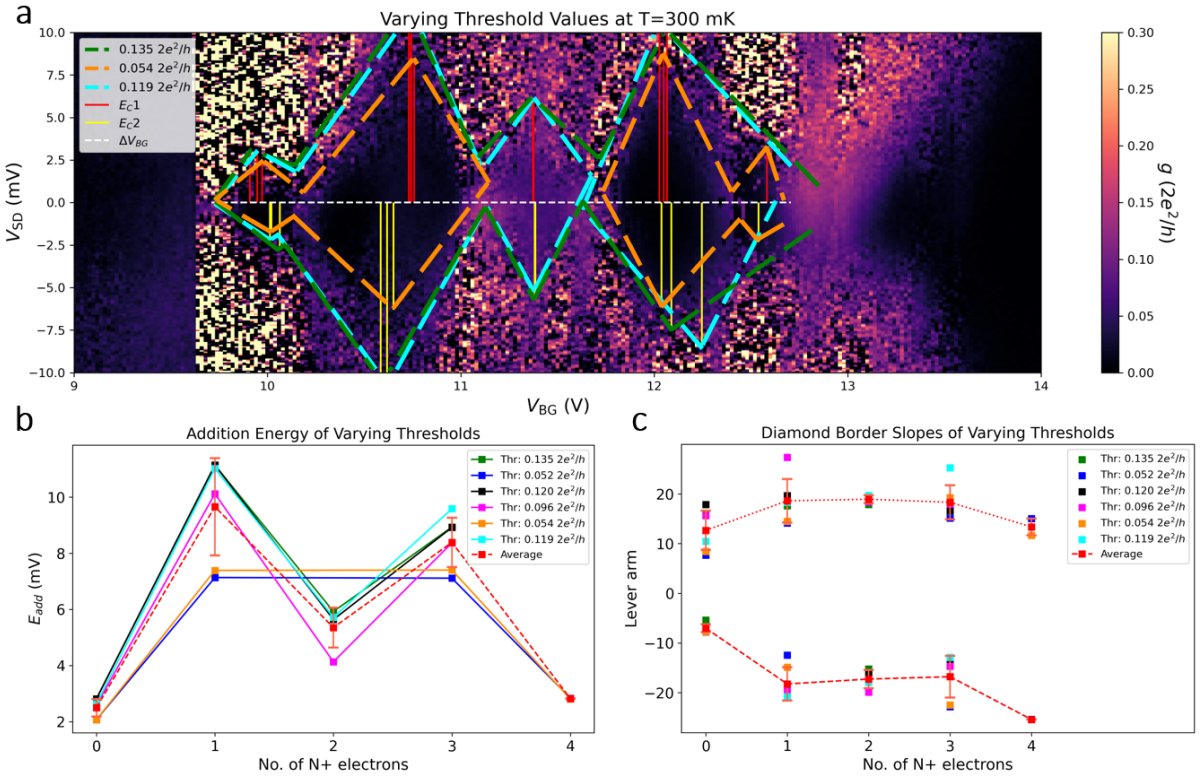

Fig. 35: Caption

15.5 to 20 V.

To this point several reasons has been mentioned which could contribute to the noise seen in the diamond plots, which makes it difficult to properly estimate the sizes and shapes of the diamonds. Varying the conductance saturation also changes the visibility of the diamonds. See Appendix for such an example. Using the zero bias sweep traces in **Fig. 34** and fitting gaussians to each conductance peak in order to extract amplitude conductance values, we get six different conductance threshold values. Using these values to 'search' for the borders of the diamonds result in diamonds of varying shape and sizes as depicted in **Fig. 35**.

In **(a)** three of the six types of threshold values and their corresponding diamond fits are on display. The remaining three has been omitted due to an increased clustering limiting the view. The extracted addition energies E_{add}, and slopes of each diamond is on view in **(b)** and **(c)** along with their average value which is displayed in red with dashed lines to guide the eye. The shapes of the diamonds exhibit remarkable addition energy variations which is typical indication of an even-odd characteristic of spin-degeneracy[4]. This would imply a observing of excited quantized states. However, for such energies to be observable the broadening of conductance resonances has to be smaller than the level-spacing $\Gamma < \Delta E$, in which, as seen in the previous section 8.2.2, does not seem to be the case due to the coupling strength. It obviously begs the question as to why the

diamonds vary in shapes and sizes. If the level spacing indeed is not the cause of the variations, then it can be assumed to be vanishing, meaning the addition energy only consists of the charging energy $E_{add} = E_C$. As it turns out, if we utilize the charging energy to estimate the size of the conducting channel responsible for the pattern observed in **Fig. 35 (a)**, using the self-capacitance of a flat disc given by,

$$C_{FlatDisc} = 8\epsilon_r\epsilon_0 R \tag{6}$$

where ϵ_r and ϵ_0 are the dielectric constant of the surrounding medium and the vacuum permittivity, respectively; and R being the size of the capacitor. Combining the charging energy $E_C = \frac{e^2}{C}$, where C is the total capacitance experienced by the device, with the Eq. 6, one can estimate the size of the channel responsible for the size of the diamond. Applying this to the average value of the addition energy of each diamond as resolved by the diamond-border algorithm, we get the following sizes: $R_{D1} = 230.70 \pm 29$ nm; $R_{D2} = 60 \pm 11$ nm; $R_{D3} = 109 \pm 14$ nm; $R_{D4} = 69 \pm 7$ nm; and $R_{D5} = 206 \pm 1$ nm, respectively. Here the subscript indicates which diamond the size has been estimated from (counting from left to right).

Although these values seem arbitrary and without any correlation, it is still striking that if one were to measure the distance of the different dimensions of the device in question, it is possible to actually relate the estimated sizes to actual device lengths. Starting with the size estimated from the first diamond and working our way up, the actual sizes has been measured to be the following: $R_{RgtMb} = 232 \pm 2$ nm; $R_{SMb} = 63 \pm 2$ nm; $R_{SD} = 111 \pm 2$ nm; $R_{DMb} = 74 \pm 2$ nm; and $R_{LftMb} = 205 \pm 2$ nm, respectively. These measured distances correspond to the following: R_{RgtMb} as the far right end of the wire structure to the middle fracture (denoted as Mb; short for the "middle barrier"), as observed and already addressed in Section 8.2.1, **Fig. 31** (see the white arrow). The size R_{SMb} is the distance from the source (left-hand lead) to the middle barrier; R_{SD} being the distance from the source to drain (i.e. the entire distance from the left to the right lead); R_{DMb} is the distance from the drain (i.e. right-hand lead) to the middle barrier; and finally R_{LftMb} is the distance from the far left end of the wire-structure to the middle barrier. See Appendix for the device marked with the various distances. It should also be noted that the uncertainties of the capacitance-estimated sizes are determined through standard error propagation applied to the combined expression of Eq. 6 and the charging energy; while the errors of the measured distances all are identical due to an approximated uncertainty related to moving the tracing line one or two pixels at each point.

Even though strain and disorder potentially could result in the emergence of accidental quantum dots[37, 4], another explanation is the formation of gate-induced potential barriers at the contacts[26].

To further show that the size variations are due to various quantum dots formation, and not as a consequence of spin-degeneracy, the difference of alternating diamond heights are in the range of 3 mV to 7 mV. This means in general the charging energy is less than previously estimated, which would result in smaller conducting channels, that would otherwise not be discernable. In addition, it would also mean that the coupling strength would be less than estimated previously, which as it appeared are much larger than the allegedly level-spacings. Furthermore, the width (138 ± 2 nm) and longitudinal dimensions, as already addressed, of the device are all longer than the Bohr-radius for InAs $a_B^* = 30$ nm, effectively meaning that there are no visible nor size-determined quantum dots in the current system where the level-spacing becomes the dominating energy scale[19]. Hence, it is the Coulomb interactions that dominates rather than confinement.

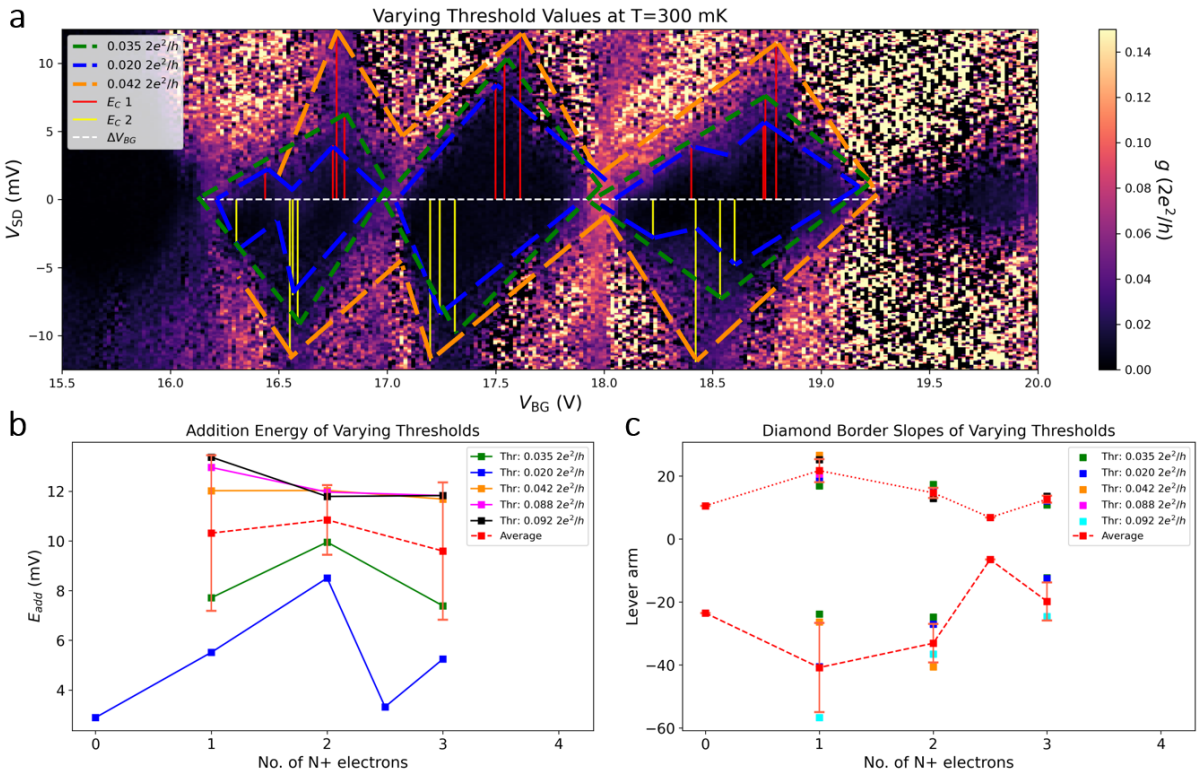

Fig. 36: Caption

As a minor comment, in **Fig. 35 (c)** the lever arms of the negative and positive kinds, both appear to be rather constant, and with close to similar absolute values for both of each diamond, indicating that at current gate voltages (9 to 14 V), each lead couples to the quantized energy levels with more-or-less equal strength.

Applying the same kind of analysis to the gate range 15.5 to 20 V, we get results as those seen in **Fig. 36**. Going through the same analysis as previously, we observe a complete different pattern of diamonds. The shapes are slanted; meaning one of the leads couples with higher affinity to the energy levels of the dot. There is no similar alternating diamond size variation; indicating that the gating seem to have less of gate-voltage correlation to the sizes, which could be explained as an increase in barrier transmission probability of some of the dots. Consequently, the slightly disappearance of the smaller-looking dots could be the result of the barrier transmission increasing. The trend of increasing sizes with increasing threshold values, as seen in **(b)**, is some-what in contrast to the diamonds at gate-voltage range of 9 to 15 V, where some of the diamonds would seem to stop growing even for larger thresholds.

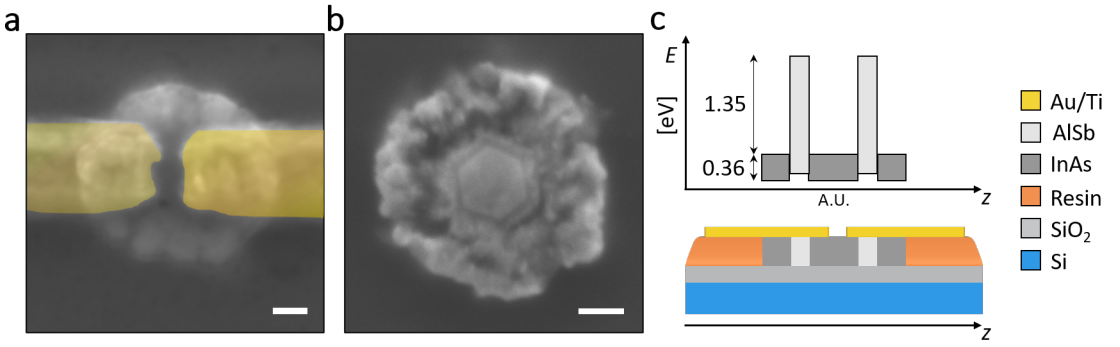

Fig. 37: InAs/AlSb/InAs heterostructure. The device is shown in (a), with a corresponding SEM image in (b). In (c) is a schematic depicted of the band diagram, as well as a graphical depiction of the device.

8.3 Fabry-Pérot Signature in InAs/AlSb/InAs Nanowire Heterostructure

Having in the previous section discussed the coulomb blockade effect in quantum dots due to single-electron tunneling between barriers of weak coupling between the leads and NC, a different quantum phenomena is observed, which to large extend differs mostly due to stronger leads-NC couplings. In this context we talk about close and open quantum dots, respectively.

In contrast to the case of closed quantum dots, in open quantum dots the leads-NC coupling surpasses the charging energy of the system $\Gamma > E_C$[21], which effectively broadens the conductance resonances to a point of where charging effects no longer dominates the system. Although the broadening results in increased transmission probability across barriers, the electron waves are likely to interfere in-between a set of barriers due to scattering off of them.

The occurrence of such events are analogous to the optical Fabry-Pérot interferometer[9] in which electron waveguides reflect off abrupt mirror-like interfaces resulting in waveguides interference inside of the cavity.

In **Fig. 37** is a device consisting of a cross-sectioned InAs/AlSb/InAs heterostructure nanowire slab of expected thickness 100 nm. The Au/Ti (200/5 nm) electrodes defined by electron lithography have an approximate distance to each other of 80 nm as determined using SEM. In **Fig. (b)** a different NC than the one used for device fabrication is seen. As is clear from the SEM image, the heterostructure exhibit a strangely looking outer shell, but do consist of a hexagonally shaped InAs core with an AlSb inner shell. The structure is representative for this growth with an approximate core diameter of 144 nm; inner AlSb shell thickness of 19 nm, and outer shell 146 nm, These values varies slightly from each individual NC. In **(c)** is depicted an illustration of both the two-terminal device geometry, and the band diagram of the structure with energy band gaps for InAs of 0.36 eV, and for AlSb the conduction band is 1.61 eV above the valence band, resulting in a large conduction band offset of 1.35 eV above that of InAs between the two materials[28].

Ohmic contact to the shown device was achieved with a resistance of 20 kΩ at room temperature. At 2.6 K the device exhibited transport as seen in **Fig. 38**. In **(a)** is shown zero-bias conductance vs. backgate voltage. Unfortunately, there was a lack of sweeps in this particular gate region of

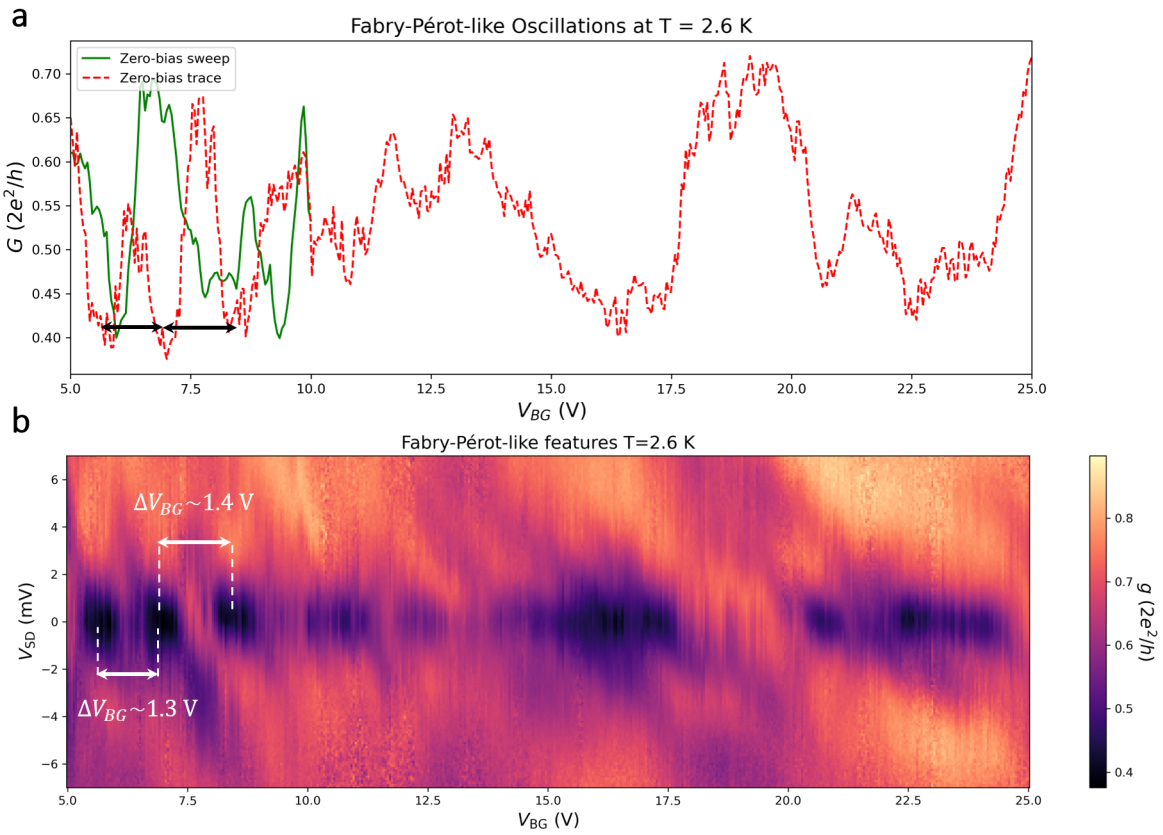

Fig. 38: Fabry-Pérot-like feature. In (a) is shown a conductance trace at zero bias voltage of the bias-spectroscopy plot in (b), as well as a conductance versus backgate of an actual measurement, shown in green. The arrows in either plot (a,b) indicate a small range of quasi-periodicity exhibiting similar backgate periods of ~ 1.3V.

5-25 V, hence the zero-bias trace of raw data points obtained from **(b)** is displayed along the three occurring conductance dips close to gate voltage of 5 V. The system did exhibit some hysteresis, which can be seen in the trace data. However, the actual measurement (green) from 5 V to 10 V does show the occurrence of four resonance amplitudes with three dips in conductance.

Such oscillations of alternating resonance amplitudes and conductance dips which does not reach zero, or reach close to zero like in the cases of closed quantum dots, is a feature of Fabry-Pérot interference due to stronger coupling than for closed quantum dots. The stronger coupling means that the resonances broadens and a background conductance appear. In this case the background conductance is a little less than 0.4 $2e^2/h$, and reaches a maximum value of around 0.8 $2e^2/h$, indicating that transport probably consists of 1D degenerate subband charge carriers[26]. The positive backgate probably indicates electron-based transport as the asymmetric electric field bends the conduction band of InAs such that electron charge carriers can occupy the conduction band and contribute to transport[15]. Pinch-off was not observed even for large negative backgate voltages: Reaching -70 V, though it is possible such phenomena was missed. See the poor resolution of **Fig. 38 (a)**, it is likely that the resolution made it more difficult to observe it.

The oscillations as seen in **(b)** with a finite background conductance is indication of Fabry-Perot interference, however it is not a typical checkerboard pattern as is normally reported for such phenomena[15], [26], [21], [41], where the pattern has pronounced conductance oscillations with quasi-periodicity and is modulated by both the gate and bias voltages. Here there is some indication of quasi-periodicity with the three resonances in **Fig. 38 (a)** and **(b)** having similar gate-spacings of $\Delta V_{BG} = 1.3$ V, however since it is taken from only two resonance dips, then it is likely not representative for the system. Additionally, the variations of conductance dips at zero bias voltage, and the lack of dark lines in V_{SD}-V_{BG} space could indicate disorder to some extend affecting the manner in which electron propagates through the device[31]; impurities on the surface could potentially lead increased backscattering impacting the background conductance[26].

9 Conclusion

In conclusion, nanocrystals are not a particularly new means of investigating or characterizing the structure from a material perspective, however when it comes to device fabrication nothing much has been reported on them. Thus, the nancrystal platform for device fabrication can have many unknown issues just waiting to be discovered and eliminated. The work done here illustrates that point of uncharted territory. As an example, while an aged and/or contaminated epoxy resin mixture is still usable for cutting sections with the microtome, it is not so for a subsequent device fabrication step. If the aim is to characterize the cross-sections by means of material charaterization tools, then it still works. Nevertheless, the improved understanding of the nanocrystal platform by means of ashing times, and perhaps also heating, is the first step towards reliable device fabrication. At present stage, the findings still have to be put to the test.

Moreover, the devices that did work never exhibited any form of representability, maybe except for the InA/AlSb/InAs, although the succesfull outcome of that device fabrication round was limited to that single device. The device exhibiting noisy quantum dot signatures was a device consisting of fractured and broken NCs likely due to the cutting direction being parallel the long axis of the structure. It is also suspected that this is indeed why it worked, as the fractures could pierce through any residuals lying on their surfaces.

As it stands, with the current knowledge of the nanocrystals, the fabrication prospects appear promising, as epoxy no longer shows sign of ashing resistance. The effect of heating the lamella has on device fabrication is still unresolved. Nevertheless, in that regard, hardening the resist by means of vacuum is an alternative.

10 Outlook

The reliably fabricated device is potentially still elusive, however if the issues has been solved, then fabrication of the investigated NC structures in this work still needs to be fabricated and characterized.

On the other hand, as this is a new platform for devices, it possesses the potential to be combined with other materials. Even just combining it with atomic layer deposited films to passivate the surface to enhance the electronic properties could be of interest.

11 Appendix

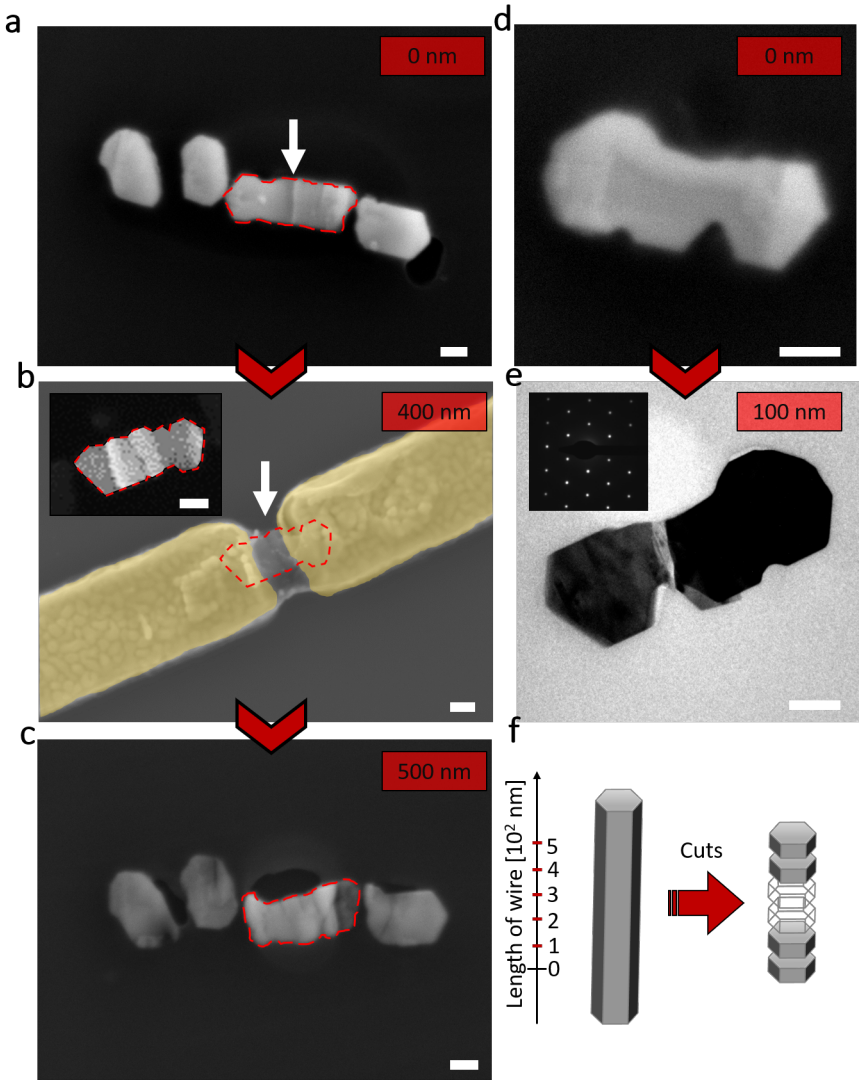

Fig. 39: Caption

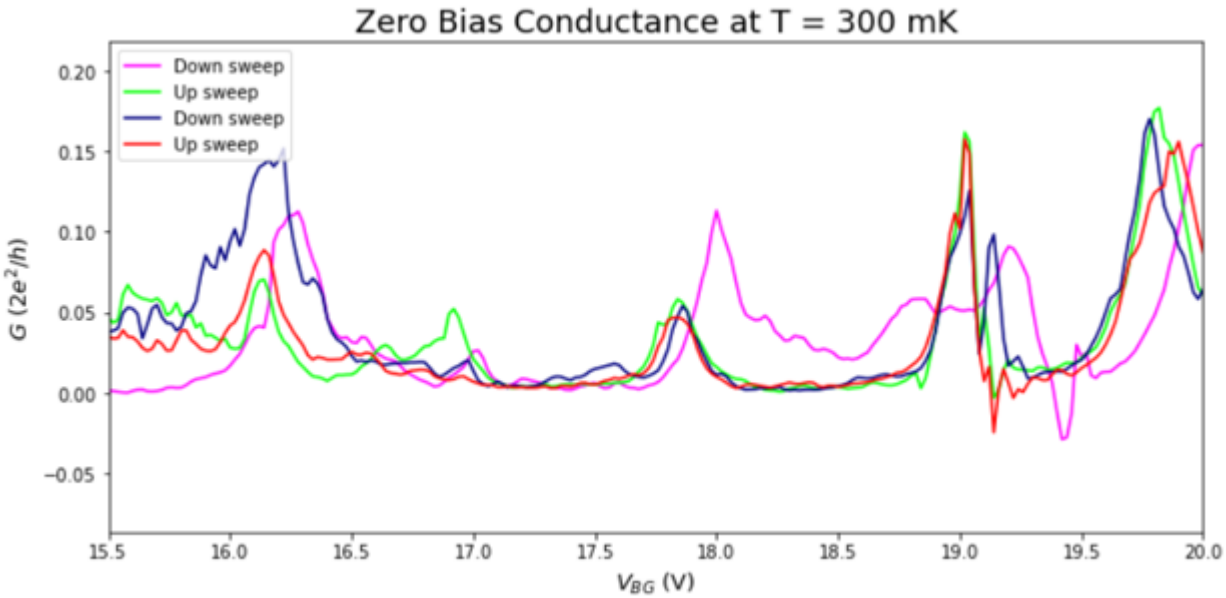

Fig. 40: Caption

References

[1] Omer Arif, Valentina Zannier, Ang Li, Francesca Rossi, Daniele Ercolani, Fabio Beltram, and Lucia Sorba. Growth and Strain Relaxation Mechanisms of InAs/InP/GaAsSb Core-Dual-Shell Nanowires. *Cryst. Growth. Des.*, 20(2):1088–1096, 2020.

[2] R. J. Barlow. *Statistics: A Guide to the Use of Statistical Methods in the Physical Sciences*. Manchester Physics Series. Wiley, 1989.

[3] Enrique Barrigón, Magnus Heurlin, Zhaoxia Bi, Bo Monemar, and Lars Samuelson. Synthesis and applications of iii–v nanowires. *Chem. Rev.*, 119(15):9170–9220, 2019.

[4] Mikael T. Björk, Claes Thelander, Adam E. Hansen, Linus E. Jensen, Magnus W. Larsson, L. Reine Wallenberg, and Lars Samuelsen. Few-Electron Quantum Dots in Nanowires. *Nano Letters*, 4(9):1621–1625, 2004.

[5] Christina Boukouvala, Joshua Daniel, and Emilie Ringe. Approaches to modelling the shape of nanocrystals. *Nano Convergence*, 8(26), 2021.

[6] Niraj Chawake, N. T. B. N. Koundinya, Sanjay Kashyap, Ajeet K. Srivastav, Devinder Yadav, R. A. Mondal, and Ravi SankarKottada. Formation of amorphous alumina during sintering of nanocrystalline B2 aluminides. *Materials Characterization*, 119:186–194, 2016.

[7] Sonia Conesa-Boj, Francesca Boioli, Eleonora Russo-Averchi, Sylvain Dunand, Martin Heiss, Daniel Ruffer, Nicolas Wyrsch, Christophe Ballif, Leo Miglio, and Anna Fontcuberta i Morral.

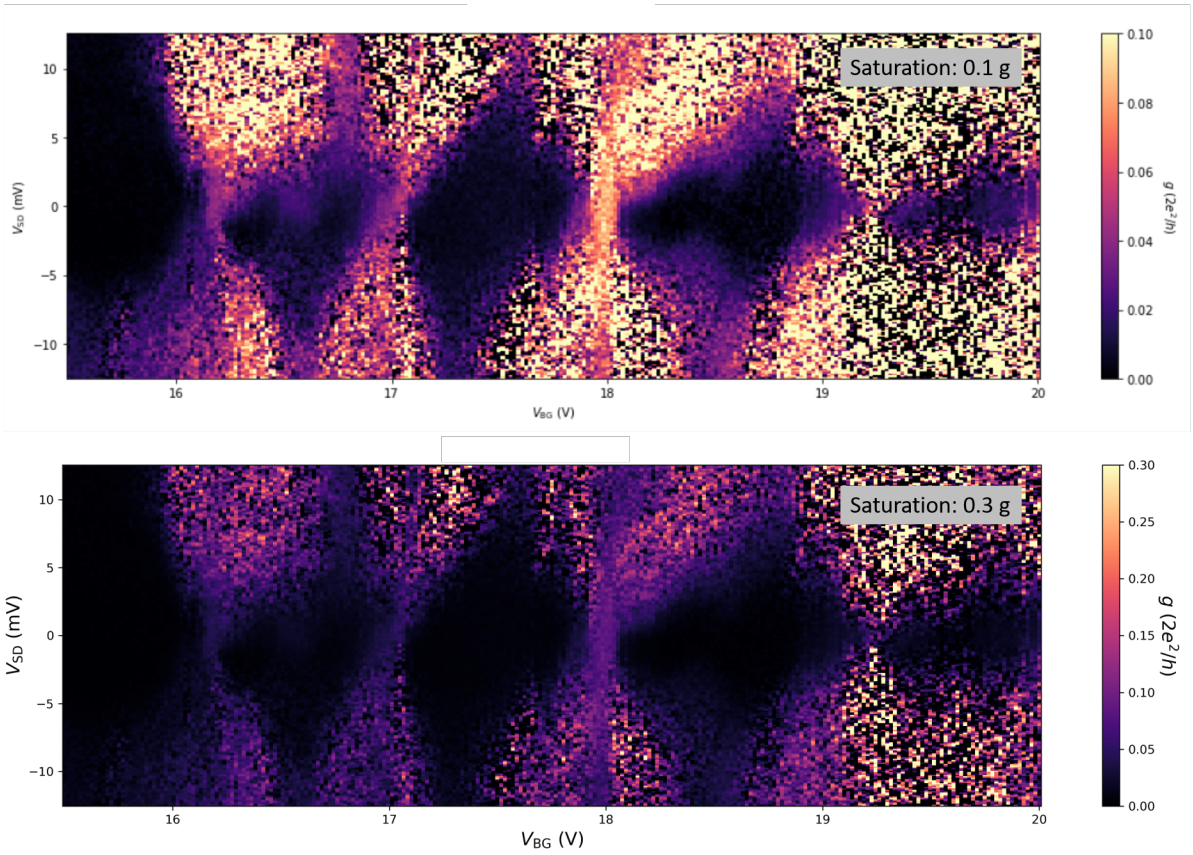

Fig. 41: Caption

Plastic and Elastic Strain Fields in GaAs/Si Core–Shell Nanowires. *Nano Lett.*, 14(4):1859–1864, 2014.

[8] Jesús A. del Alamo. Nanometre-scale electronics with iii–v compound semiconductors. *Nature*, 479:317–323, 2011.

[9] Xiangfeng Duan, Yu Huang, Ritesh Agarwal, and Charles M. Lieber. Single-nanowire electrically driven laser. *Nature*, 421:241–245, 2003.

[10] Vladimir G. Dubrovskii. *Nucleation Theory and Growth of Nanostructures*. NanoScience and Technology. Springer Berlin, Heidelberg, 2014.

[11] J. W. Edington. *Electron Diffraction in the Electron Microscope*. Red Globe Press London, 1975.

[12] Zhuo Fang, Yongda Yan, and Yanquan Geng. Recent Progress in the Nanoskiving Approach: A Review of Methodology, Devices and Applications. *Adv. Mater. Technol.*, 6(12):2100477, 2021.

[13] Tiago Ferreia and Wayne Rasband. Imagej user guide.

[14] Audrey M. Glauert and Peter R. Lewis. *Biological Specimen Preparation for Transmission Electron Microscopy*, chapter 6. Princeton Legacy Library, 2016.

[15] Kasper Grove-Rasmussen, Henrik Ingerslev Jørgensen, and Poul Erik Lindelof. Fabry-Perot interference, Kondo effect and Coulomb blockade in carbon nanotubes. *Physica E.*, 40(1):92–98, 2007.

[16] D. Hall and D. J. Bacon. *Introduction to Dislocations*. Elsevier Ltd., 2001.

[17] Simon Hettler, Manuel Dries, Peter Hermann, Martin Obermair, Dagmar Gerthsen, and Marek Malac. Carbon contamination in scanning transmission electron microscopy and its impact on phase-plate applications. *Micron*, 96:38–47, 2017.

[18] P. Hirsch, M. Kässens, M. Pûttmann, and L. Reimer. Contamination in a scanning electron microscope and the influence of specimen cooling. *Scanning*, 16:101–110, 1994.

[19] Thomas Ihn. *Semiconductor Nanostructures - Quantum States and Electronic Transport*. Oxford University Press, 2013.

[20] L. P. H. Jeurgens, W. G. Sloof, F. D. Tichelaar, and E. J. Mittemeijer. Thermodynamic stability of amorphous oxide films on metals: Application to aluminum oxide films on aluminum substrates. *Physical Review B.*, 62(7):4707, 2000.

[21] H. I. Jørgensen, K. Grove-Rasmussen, T. Novotny, K. Flensberg, and P. E. Lindelof. Electron Transport in Single-Wall Carbon Nanotube Weak Links in the Fabry-Pérot Regime. *Physical Review Letters*, 96(20):207003–1–207003–4, 2006.

[22] Thomas Kanne, Mikelis Marnauza, Dags Olsteins, Damon J. Carrad, Joachim E. Sestoft, Joeri de Bruijckere, Lunjie Zeng, Erik Johnson, Eva Olsson, Kasper Grove-Rasmussen, and Jesper Nygård. Epitaxial Pb on InAs nanowires for quantum devices. *Nat. Nanotechnol.*, 16:776–781, 2021.

[23] Anirudha Karati, M. Vaidya, and B. S. Murty. Comparison of Different Processing Routes for the Synthesis of Semiconducting AlSb. *J. of Materi. Eng. and Perform.*, 27:6196–6205, 2018.

[24] Hanna Kindlund, Reza R. Zamani, Axel R. Persson, Sebastian Lehmann, L. Reine Wallenberg, and Kimberly A. Dick. Kinetic Engineering of Wurtzite and Zinc-Blende AlSb Shells on InAs Nanowires. *Nano Lett.*, 18(9):5775–5781, 2018.

[25] Leo P. Kouwenhoven and Paul L. McEuen. *Single Electron Transport Through a Quantum Dot. In: Timp, G. (eds) Nanotechnology*, chapter 13. Springer, 1999.

[26] Andrey V. Kretinin, Ronit Popovitz-Biro, Diana Mahalu, and Hadas Shtrikman. Multimode Fabry-Pérot Conductance Oscillations in Suspended Stacking-Faults-Free InAs Nanowires. *Nano Lett.*, 10(9):3439–3445, 2010.

[27] Dominik Kriegner, Christian Panse, Bernhard Mandl, Kimberly A. Dick, Mario Keplinger, Johan M. Persson, Philippe Caroff, Daniele Ercolani, Lucia Sorba, Friedhelm Bechstedt, Julian Stangl, and Gunther Bauer. Unit Cell Structure of Crystal Polytypes in InAs and InSb Nanowires. *Nano Lett.*, 11(4):1483–1489, 2011.

[28] Herbert Kroemer. The 6.1 Å family (InAs, GaSb, AlSb) and its heterostructures; a selective review. *Physica E*, 20:196–203, 2004.

[29] Sergey Lazarev, David J. O. Goransson, MAgnus Borgstrom, Messing MAria E, H. Q. Xu, Dmitry Dzhigaev, Oleksander M. Yefanov, Sondes Bauer, Tilo Baumbach, and Robert Feidenhans'I. Revealing misfit dislocations in InAsxP1x-InP core–shell nanowires by x-ray diffraction. *Nanotechnology*, 30(50):505703, 2017.

[30] Handong Li, Hayfaa Alradhi, Zhiming Jin, Ezekiel A. Anyebe, Ana M. Sanchez, Wojcioech M. Linhart, Robert Kudrawiec, Hehai Fang, Zhiming Wang, Weida Hu, and Qiandong Zhuang. Novel Type-II InAs/AlSb Core–Shell Nanowires and Their Enhanced Negative Photocurrent for Efficient Photodetection. *Physical Review B.*, 28(8):1705382, 2017.

[31] Wenjie Liang, Marc Bockrath, Dolores Bozovic, Jason H. Hafner, M. Tinkham, and Hongkun Park. Fabry-Perot interference in a nanotube electron waveguide. *Nature*, 411:665–669, 2001.

[32] Yung-Chan Lin, Hyun Goo Ji, Li-Jen Chang, Yao-Pang Chan, Zheng Liu, Gun-Do Lee, Po-Wen Chiu, Hiroki Ago, and Kazu Suenaga. Scanning Moiré Fringe Method: A Superior Approach to Perceive Defects, Interfaces, and Distortion in 2D Materials. *ACS Nano*, 14(5):6034–6042, 2020.

[33] Yan Lu, Sisi Xiang, Lirong Xiao, Lihua Wang, Qingsong Deng, Ze Zhang, and Xiaodong Han. Dislocation "Bubble-Like-Effect" and the Ambient Temperature Super-plastic Elongation of Body-centred Cubic Single Crystalline Molybdenum. *Scientific Reports*, 6:22937, 2016.

[34] M. Murayama and T. Nakayama. Chemical trend of band offsets at wurtzite/zinc-blende heterocrystalline semiconductor interfaces. *Phys. Rev. B*, 49:4710, 1994.

[35] Chanh Nguyen, Berinder Brar, Herbert Kroemer, and John H. English. Surface donor contribution to electron sheet concentrations in not-intentionally doped InAs-AlSb quantum wells. *Appl. Phys. Lett.*, 60(1854), 1992.

[36] J. Nicolai, Ch. Gatel, B. Warot-Fonrose, R. Teissier, A. N. Baranov, C. Magen, and A. Ponchet. Elastic strains at interfaces in InAs/AlSb multilayer structures for quantum cascade lasers. *Appl. Phys. Lett.*, 104(031907), 2014.

[37] J. Nygård, D. H. Cobden, M. Bockrath, P. L. McEuen, and P. E. Lindelof. Electrical transport measurement on single-walled carbon nanotubes. *Applied Physics A*, 69:297–304, 1999.

[38] M. Pierre, R. Wacquez, X. Jehl, M. Sanquer, M. Vinet, and O. Cueto. Single-donor ionization energies in a nanoscale CMOS channel. *Nature Nanotechnology*, 5:133–137, 2010.

[39] Louis A. Pilato and Michael J. Michno. *Advanced Composite Materials*. Springer Berlin, Heidelberg, 1994.

[40] M. P. J. Punkkinen, P. Laukkanen, J. Lång, M. Kuzmin, M. Tuominen, V. Tuominen, J. Dahl, M. Pessa, M. Guina, K. Kokko, J. Sadowski, B. Johansson, I. J. Väyrynen, and L. Vitos. Oxidized in-containing iii-v(100) surfaces: Formation of crystalline oxide films and semiconductor-oxide interfaces. *Phys. Rev. B.*, 83:195329, 2011.

[41] Joachim E. Sestoft, Aske N. Gejl, Thomas Kanne, Rasmus D. Schlosser, Daniel Ross, Daniel Kjær, Kasper Grove-Rasmussen, and Jesper Nygård. Scalable Platform for Nanocrystal-Based Quantum Electronics. *Adv. Funct. Mater.*, 32(28):2112941, 2022.

[42] Huaping Sheng, He Zheng, Fan Cao, Shujing Wu, Lei Li, Chun Liu, and Dongshan Zhao Jianbo Wang. Anelasticity of twinned CuO nanowires. *Nano Research*, 8(11):3687–3693, 2015.

[43] J. Spitzer, A. Höpner, M. Kuball, M. Cardona, B. Jenichen, H. Neuroth, B. Brar, and H. Kroemer. Influence of the interface composition of InAs/AlSb superlattices on their optical and structural properties. *Journal of Applied Physcs*, 77(811), 1995.

[44] Arthur R. Spurr. A low-viscosity epoxy resin embedding medium for electron microscopy. *J. Ultrastructure Res.*, 26(31):31–43, 1969.

[45] G. Stan, C. V. Ciobanu, P. M. Parthangal, and R. F. Cook. Diameter-Dependent Radial and Tangential Elastic Moduli of ZnO Nanowires. *Nano Lett.*, 7(12):3691–3697, 2007.

[46] M. D. Stiles and D. R. Hamann. Electron transmission through silicon stacking faults. *Phys. Rev. B*, 41:5280, 1990.

[47] K. Takase, corresponding author, Y. Ashikawa, G. Zhang, K. Tateno, , and S. Sasaki. Highly gate-tuneable rashba spin-orbit interaction in a gate-all-around inas nanowire metal-oxide-semiconductor field-effect transistor. *Scientific Reports*, 7:930, 2017.

[48] Hongxiang Teng, Kotaro Koike, Dingying Zhou, Zen Satoh, Yasuhiro Koike, and Yoshiyuki Okamoto. High glass transition temperatures of poly(methyl methacrylate) prepared by free radical initiators. *J. Polym. Sci. A Polym. Chem.*, 47:315–317, 2009.

[49] Gary Tuttle, Herbert Kroemer, and John H. English. Electron concentrations and mobilities in AlSb/InAs/AlSb quantum wells. *Journal of Applied Physics*, 65(5239), 1989.

[50] Gary Tuttle, Herbert Kroemer, and John H. English. Effects of interface layer sequencing on the transport properties of InAs/AlSb quantum wells: Evidence for antisite donors at the InAs/AlSb interface. *Journal of Applied Physcs*, 67(3032), 1990.

[51] Jintao Wan, Cheng Li, Zhi-Yang Bu, Hong Fan, and Bo-Geng Li. Acrylonitrile-capped poly(propyleneimine) dendrimer curing agent for epoxy resins: Model-free isoconversional curing kinetics, thermal decomposition and mechanical properties. *Materials Chemistry and Physics*, 138(1):303–312, 2013.

[52] Jintao Wan, Cheng Li, Zhi-Yang Bu, Hong Fan, and Bo-Geng Li. Evaluating a four-directional benzene-centered aliphatic polyamine curing agent for epoxy resins. *Journal of Thermal Analysis and Calorimetry*, 114:365–375, 2013.

[53] Jinghui Wang, Xin Gao, Yuanhong Cai, Zhihao Wang, Zhongliang Qiao, and Baoxue Bo. The photoluminescence characteristics of gaas surface by plasma treatment. *Materials Science in Semiconductor Processing*, 134:106050, 2021.

[54] Lihua Wang, Deli Kong, Yin Zhang, Lirong Xiao, Yan Lu, Zhigang Chen, Ze Zhang, Jin Zou, Ting Zhu, and Xiaodong Han. Mechanically Driven Grain Boundary Formation in Nickel Nanowires. *ACS Nano*, 11(12):12500–12508, 2017.

[55] Xudong Wang, Jinhui Song, and Zhong Lin Wang. Direct-Current Nanogenerator Driven by Ultrasonic Waves. *Science*, 316(5821):102–105, 2007.

[56] Douglas C Watson, Ramses V Martinez, Yannik Fontana, Eleonora Russo-Averchi, Martin Heiss, Anna Fontcuberta i Morral, George M Whitesides, and Marko Lončar. Nanoskiving core-shell nanowires: a new fabrication method for nano-optics. *Nano Lett.*, 14(2):524–531, 2014.

[57] Jianan Yang, Gerold W. Neudeck, and John P. Denton. Electrical Effects of a Single Stacking Fault on Fully Depleted Thin-Film Silicon-on-Insulator P-Channel Metal-Oxide-Semiconductor Field-Effect Transistors. *Journal of Applied Physics*, 91(420), 2002.

[58] Yunyan Zhang, Jiang Wu1, Martin Aagesen, and Huiyun Liu. Iii–v nanowires and nanowire optoelectronic devices. *J. Phys. D*, 48:463001, 2015.